

A Disease-Centric Vision-Language Foundation Model for Precision Oncology in Kidney Cancer

Yuhui Tao^{1,2†}, Zhongwei Zhao^{3†}, Zilong Wang^{4†}, Xufang Luo^{4†},
Feng Chen^{5†}, Kang Wang^{1,2}, Chuanfu Wu^{6,7}, Xue Zhang⁸,
Shaoting Zhang⁹, Jiayi Yao¹⁰, Xingwei Jin¹¹, Xinyang Jiang⁴,
Yifan Yang⁴, Dongsheng Li⁴, Lili Qiu⁴, Zhiqiang Shao^{12*},
Jianming Guo^{13*}, Nengwang Yu^{3*}, Shuo Wang^{1,2*}, Ying Xiong^{13*}

^{1*}Digital Medical Research Center, School of Basic Medical Sciences, Fudan University, Shanghai, 200032, China.

^{2*}Shanghai Key Laboratory of Medical Imaging Computing and Computer Assisted Intervention, Shanghai, 200032, China.

^{3*}Department of Urology, Qilu Hospital of Shandong University, Jinan, Shandong, 250012, China.

⁴Microsoft Research Asia, Shanghai, 200232, China.

⁵Department of Radiology, The First Affiliated Hospital, Zhejiang University School of Medicine, Hangzhou, 310006, China.

⁶Center of Health data science, Linyi People's Hospital, Shandong, 276003, China.

⁷Shandong Open Laboratory of Data Innovation Application, Shandong, 276003, China.

⁸Department of Radiology, the First People's Hospital of Lianyungang, Lianyungang, 222002, China.

⁹Department of Radiology, Shandong Cancer Hospital and Institute, Shandong First Medical University and Shandong Academy of Medical Sciences, Jinan, 250117, China.

¹⁰Department of Urology, Zhangye People's Hospital affiliated to Hexi University, Zhangye, 734000, China.

¹¹Department of Urology, Ruijin Hospital, Shanghai Jiao Tong University School of Medicine, Shanghai, 200025, China.

^{12*}Department of Urology, Linyi People's Hospital, Shandong, 276003, China.

^{13*}Department of Urology, Zhongshan Hospital, Fudan University, Shanghai, 200032, China.

*Corresponding author(s). E-mail(s): shaozq2005@163.com;
guo.jianming@zs-hospital.sh.cn; qiluyunengwang@hotmail.com;
shuowang@fudan.edu.cn; xiong.ying@zs-hospital.sh.cn;

†These authors contributed equally to this work.

Abstract

The non-invasive assessment of increasingly incidentally discovered renal masses is a critical challenge in urologic oncology, where diagnostic uncertainty frequently leads to the overtreatment of benign or indolent tumors. While artificial intelligence (AI) models have been developed, they often lack the generalizability and deep semantic understanding required for clinical practice. In this retrospective, multicenter study, we developed and validated RenalCLIP using a dataset of 27,866 CT scans from 8,809 patients across nine Chinese medical centers and the public TCIA cohort, a visual-language foundation model for characterization, diagnosis and prognosis of renal mass. The model was developed via a two-stage pre-training strategy that first enhances the image and text encoders with domain-specific knowledge before aligning them through a contrastive learning objective, intended to create robust representations for superior generalization and diagnostic precision. RenalCLIP achieved better performance and superior generalizability across 10 core tasks spanning the full clinical workflow of kidney cancer, including anatomical assessment (R.E.N.A.L. nephrometry score), diagnostic classification (malignancy identification; invasiveness evaluation), and survival prediction (recurrence-free survival, disease-specific survival, and overall survival), compared with other state-of-the-art general-purpose CT foundation models. Especially, for complicated task like recurrence-free survival prediction in the TCIA cohort, RenalCLIP achieved a C-index of 0.726, representing a substantial improvement of approximately 20% over the leading baselines. Furthermore, RenalCLIP’s pre-training imparted remarkable data efficiency; in the diagnostic classification task, it only needs 20% training data to achieve the peak performance of all baseline models even after they were fully fine-tuned on 100% of the data. Additionally, it achieved superior performance in report generation, image-text retrieval and zero-shot diagnosis tasks. Our findings establish that a disease-centric, vision-language pre-training strategy is crucial for building powerful, generalizable, and data-efficient models for precision oncology for kidney cancer. RenalCLIP provides a robust tool with the potential to enhance diagnostic accuracy, refine prognostic stratification, and personalize the management of patients with kidney cancer.

1 Introduction

The widespread adoption of medical imaging has dramatically increased the incidental detection of renal masses, posing new clinical dilemmas in kidney cancer management. Despite a surge in radiologically identified renal tumors, kidney cancer-specific mortality has not declined in parallel, underscoring a substantial burden of overtreatment for

benign or indolent lesions^{1,2}. Notably, up to 20% of surgically resected renal masses are ultimately confirmed as benign, subjecting patients to unnecessary surgical risks, healthcare costs, and potential loss of renal function^{3,4}. Current diagnostic pathways are limited: radiological interpretation remains highly subjective with considerable inter-observer variability⁵, while percutaneous biopsy is invasive, carries a significant non-diagnostic rate, and frequently fails to capture the true biological aggressiveness of tumors due to intratumoral heterogeneity⁶⁻⁹. A critical unmet need therefore exists for a non-invasive tool that can precisely and comprehensively assess a tumor’s malignant potential, aggressiveness, and prognosis from preoperative CT scans¹⁰⁻¹⁶.

While artificial intelligence (AI) has shown promise in medical image analysis, conventional models for kidney cancer have been constrained by critical limitations that have prevented their clinical translation. Most are trained on image data alone, overlooking the rich semantic context within radiology reports that is essential for expert-level reasoning¹⁷. Furthermore, the prevailing “one-model, one-task” paradigm is inefficient and results in models that lack generalizability, often failing when tested on external data^{18,19}. Recent breakthroughs in general-purpose vision-language foundation models²⁰⁻²⁴ offer a path forward but possess a critical flaw for oncology: their broad training across all pathologies lacks the necessary depth for the nuanced, high-stakes decisions required in cancer care^{19,25-28}. A general CT model may identify an organ, but it cannot be expected to master the subtle radiological features that distinguish an indolent from an aggressive renal tumor.

We reasoned that to solve a specific clinical problem, a disease-centric strategy is essential. Such an approach, which revolves entirely around the clinical and pathological complexities of a single disease, is necessary to bridge the gap between generalist AI and the demands of precision medicine. Here, we present RenalCLIP, a multi-task, disease-centric vision-language foundation model designed for comprehensive assessment of kidney cancer. RenalCLIP was pre-trained on a large-scale, multi-institutional dataset comprising 21,819 CT series and their corresponding radiology reports from 6,867 patients, collected across four leading medical centers in China. By aligning visual representations from CT scans with clinical-pathological semantics extracted from textual reports, RenalCLIP learns robust, context-aware embeddings of renal tumors. We systematically evaluated its performance across a broad spectrum of clinically relevant tasks, including automated anatomical scoring, benign-versus-malignant discrimination, aggressiveness stratification, multi-endpoint survival prognosis, and cross-modal retrieval. In all benchmarks, RenalCLIP consistently outperformed existing state-of-the-art models. Moreover, the model demonstrated advanced capabilities in zero-shot learning and radiology report generation, underscoring its potential as a foundation model for precision kidney cancer imaging and decision support.

2 Results

2.1 Overview of RenalCLIP

A comprehensive assessment of renal masses from CT imaging, spanning their anatomical complexity, diagnosis, and long-term prognosis, is essential for guiding personalized

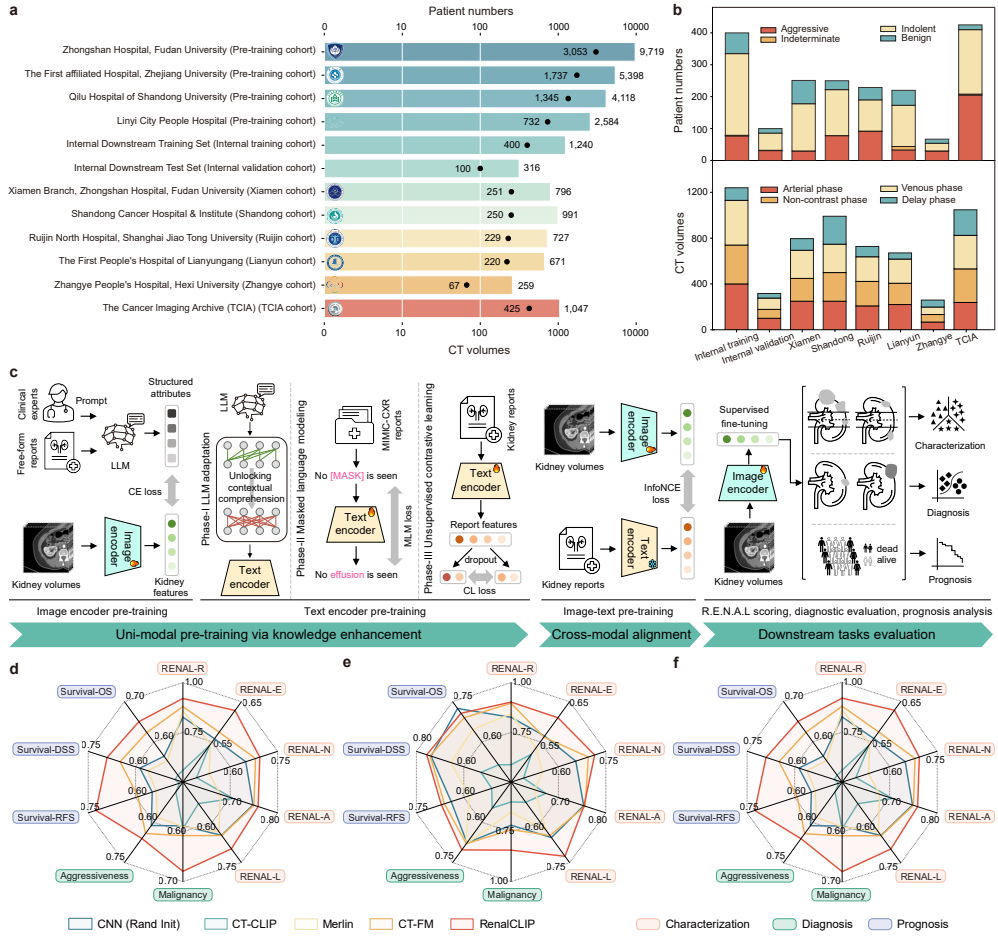


Fig. 1 | Overview of the RenalCLIP design. **a,b**, The study was developed using a large-scale, multi-center dataset. **a**, Distribution of patients and CT volumes across the pre-training, fine-tuning, and validation cohorts (dots, patients; bars, CT volumes). **b**, The cohorts encompass a diverse range of pathologic subtypes and CT phase availability, ensuring comprehensive model training and evaluation. **c**, Schematic of the RenalCLIP framework, illustrating the two-stage pre-training pipeline—involving uni-modal knowledge enhancement and cross-modal alignment—and its subsequent application to the three primary clinical downstream domains: characterization, diagnosis, and prognosis. **d–f**, Summary of model performance via radar plots, demonstrating the consistent superiority or highly competitive performance of RenalCLIP against baseline models across these primary domains. The comparison is shown for the internal test cohort (**d**), the combined external test cohort (**e**), and the TCIA cohort (**f**). In these plots, performance on characterization and diagnosis tasks is quantified by the area under the receiver operating characteristic curve (ROC AUC), while prognosis is quantified by Harrell’s C-index.

patient management. However, achieving this in a consistently accurate and objective manner remains a significant clinical challenge. To address this, we developed RenalCLIP, a disease-centric vision-language foundation model for renal cancer, by pre-training with a large-scale dataset of 21,819 CT scans from 6,867 patients. The model’s performance on a suite of downstream clinical tasks was then rigorously evaluated on a multi-center dataset of 1,942 patients (6,047 CT scans), which was partitioned into an internal cohort for fine-tuning and testing, five proprietary external cohorts (which were aggregated to form the combined external test cohort for pooled analysis), and the public Cancer Imaging Archive (TCIA)²⁹ cohort for comprehensive validation (Fig. 1a-b, Extended Data Table 1).

The pre-training of RenalCLIP is designed to explicitly embed disease-centric clinical knowledge into its encoders before their cross-modal alignment (Fig. 1c, Extended Data Fig. 1c-e). This is achieved through a crucial initial knowledge-enhancement stage. The image encoder is pre-trained within a multi-task learning framework, supervised by a rich set of structured attributes that were systematically extracted from radiology reports. Concurrently, the text encoder, built upon the Llama3 large language model³⁰, is transformed into a specialized medical language expert using LLM2Vec techniques^{31,32}. In the second stage, these knowledge-infused encoders are jointly optimized through a vision-language contrastive objective³³, forcing a deep alignment between fine-grained visual features and their clinical semantics (see Methods for a detailed description of the entire pre-training pipeline).

We then systematically benchmarked RenalCLIP’s capabilities across a comprehensive suite of 13 distinct downstream tasks. These ranged from a core set of 10 applications across three major clinical domains—renal mass characterization (five R.E.N.A.L. score components), diagnosis (malignancy and aggressiveness), and prognosis (prediction of recurrence-free survival (RFS), disease-specific survival (DSS), and overall survival (OS))—to 3 tests of advanced capabilities, namely zero-shot classification, cross-modal retrieval, and report generation. As summarized in the performance radar plots (Fig. 1d-f), RenalCLIP consistently demonstrates superior or highly competitive performance against a range of baseline models, including a standard 3D CNN³⁴ trained from scratch (termed CNN (Rand Init) in figures) and three general-purpose CT foundation models (CT-CLIP³⁵, Merlin³⁶, and CT-FM³⁷), across the three primary task domains. The detailed evidence for its superiority across all 13 tasks is presented in the subsequent sections (Figs. 2-5).

2.2 Automated anatomical characterization and report generation

The R.E.N.A.L. nephrometry score serves as a standardized framework for quantifying the anatomical complexity of renal tumors, facilitating preoperative risk stratification and surgical planning³⁸. We systematically evaluated RenalCLIP’s ability to predict the five constituent anatomical features—R (Radius), E (Exophytic/Endophytic), N (Nearness to collecting system), A (Anterior/Posterior), and L (Location) using ROC AUC as the primary metric (see Supplementary Table 1 for R.E.N.A.L. grading details). RenalCLIP’s superior discriminative performance was first evident in

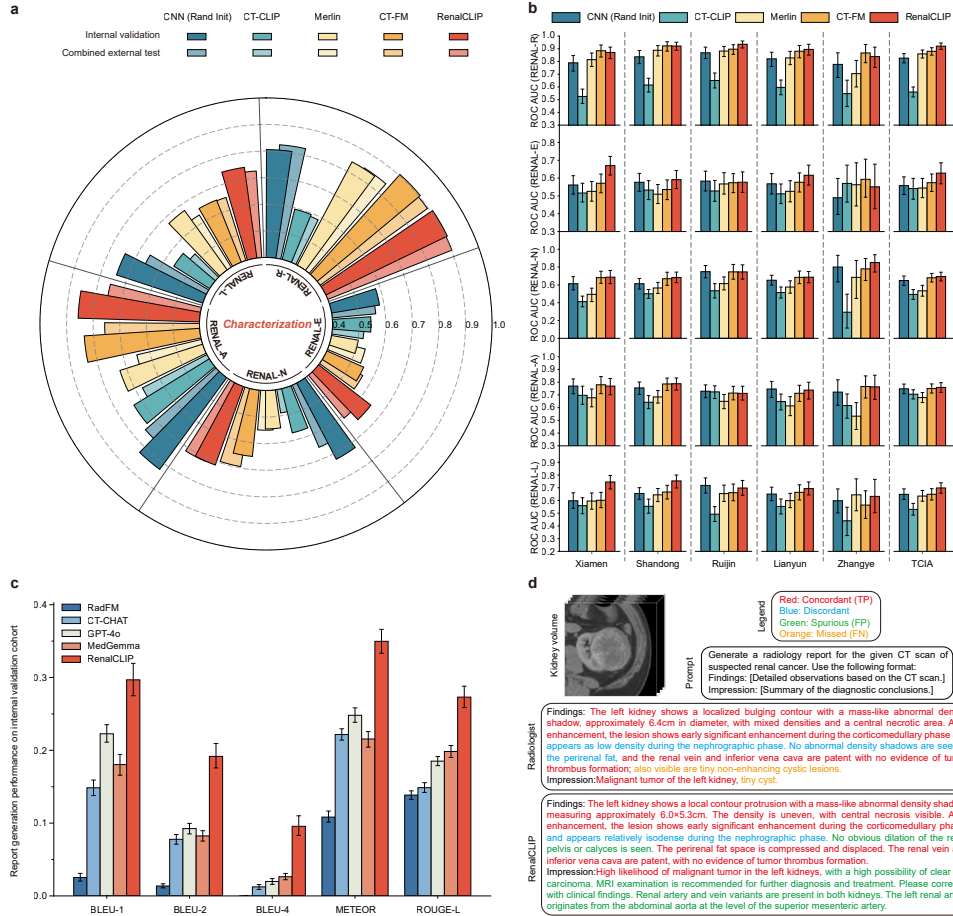


Fig. 2 | Performance of RenalCLIP on renal mass characterization. **a**, Rose plots summarizing the performance on the five R.E.N.A.L. score components show that RenalCLIP outperforms baseline models on most features in both the internal validation cohort and the combined external test cohort (comprising the Xiamen, Shandong, Ruijin, Lianyun, and Zhangye cohorts). **b**, Bar charts detailing the performance across the five proprietary external cohorts and the public TCIA cohort further demonstrate the model’s robust generalizability. **c**, For the task of radiology report generation, RenalCLIP achieves the highest scores across all standard language metrics when benchmarked against several state-of-the-art generative models. **d**, A representative qualitative example illustrates the high concordance between a report generated by RenalCLIP and the ground-truth report written by a human expert (see Extended Data Fig. 2 for comprehensive comparisons). Performance on anatomical characterization (**a**, **b**) is quantified by ROC AUC. Capped error bars in **b** and **c** represent 95% confidence intervals and the centers correspond to the computed values of each metric.

the internal validation cohort, where it outperformed all comparative models on features R (ROC AUC = 0.908), E (0.646), A (0.857), and L (0.747), while achieving a competitive ROC AUC of 0.713 on feature N (vs. 0.723 for the baseline CNN). This strong performance was largely replicated in the combined external test cohort, where it again attained the highest AUC for R (0.902), E (0.610), N (0.715), and L (0.727), while remaining competitive for feature A (0.754 vs. 0.757 for CT-FM) (Fig. 2a). Further analysis of individual external cohorts confirmed its robustness, with RenalCLIP achieving the highest ROC AUC in the majority of head-to-head comparisons across most features. Taken together, these results establish RenalCLIP’s superior and generalizable capability for automated, multi-component anatomical scoring across diverse clinical settings (Fig. 2b; see Supplementary Tables 2–6 for comprehensive results).

The radiology report is the primary communication tool for translating complex imaging findings into actionable clinical insights³⁹. We therefore evaluated RenalCLIP on the advanced task of automated report generation, which tests its ability to synthesize learned anatomical features into a coherent narrative, moving beyond the prediction of discrete scores. To this end, we benchmarked its report generation quality against state-of-the-art models, including GPT-4o⁴⁰, MedGemma⁴¹, RadFM⁴², and CT-CHAT³⁵. Across all standard language generation metrics (BLEU-1, BLEU-2, BLEU-4, METEOR, and ROUGE-L), RenalCLIP achieved the highest scores on the internal validation cohort, indicating a superior alignment with ground-truth reports annotated by expert radiologists (Fig. 2c). A representative qualitative example comparing a RenalCLIP-generated report to the human-annotated ground truth is provided in Fig. 2d, while comprehensive comparisons against all baseline models and the quantitative results are detailed in Extended Data Fig. 2 and Supplementary Tables 7–11.

2.3 Robust diagnosis of malignancy and aggressiveness stratifies patient outcomes

We first assessed RenalCLIP’s capability in diagnosing the malignancy of renal masses, a critical prerequisite for determining treatment strategies⁴³. Across both the internal and combined external validation cohorts, RenalCLIP consistently achieved the highest ROC AUC among all models (Fig. 3a). Its diagnostic precision was further evidenced in the combined external cohort, where RenalCLIP attained leading performance across five key metrics: ROC AUC (0.841), PR AUC (0.941), sensitivity (0.827), specificity (0.735), and F1-score (0.876) (Fig. 3b). This superiority was maintained across the majority of the six individual external cohorts (5 out of 6, Fig. 3c and Supplementary Table. 12). Crucially, the performance gap between RenalCLIP and the baseline models widened on the external cohorts, providing compelling evidence for its superior generalizability. While RenalCLIP outperformed the top baseline (CNN) by 8.2% in the internal cohort (0.856 vs. 0.791), this margin increased to 17.3% against CNN (0.841 vs. 0.717) and 13.8% against the leading baseline (CT-FM, 0.841 vs. 0.739) in the combined external cohort (visualized in ROC curves in Fig. 3d–e, and Extended Data Fig. 3).

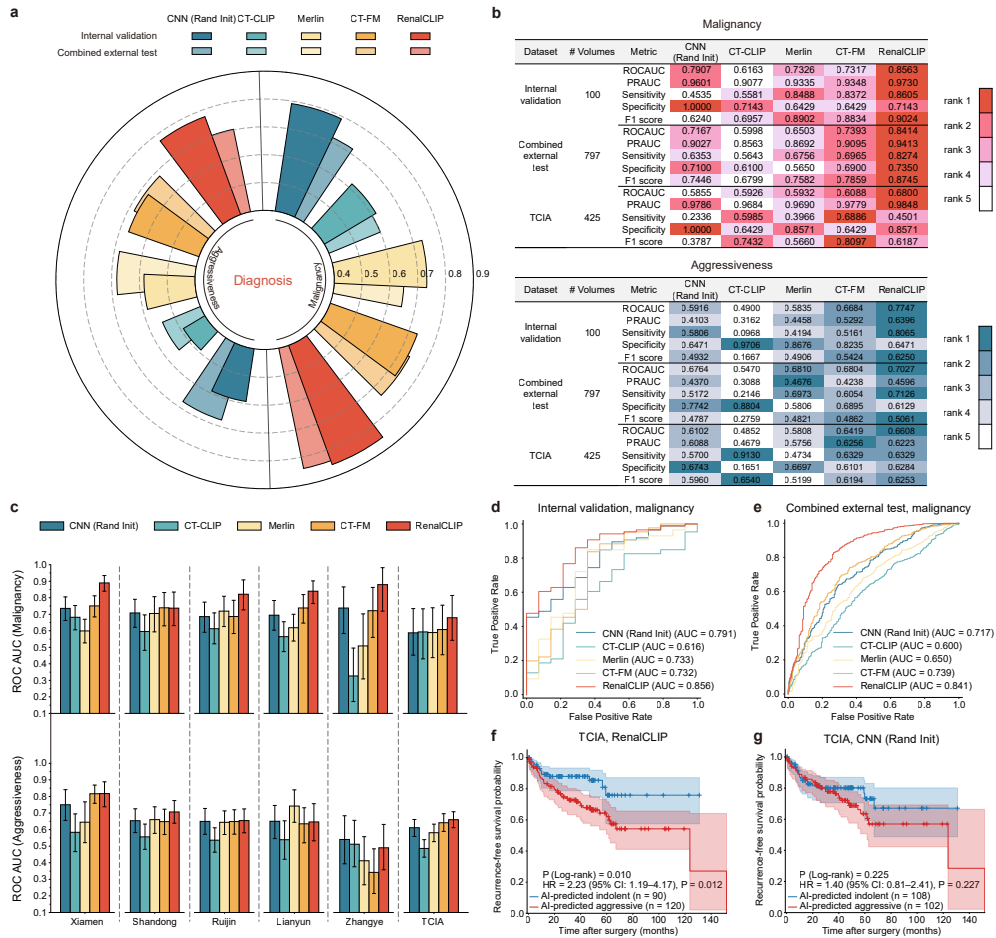


Fig. 3 | Performance of RenalCLIP on diagnosis of renal masses. a, Rose plots summarizing diagnostic performance demonstrate RenalCLIP’s superiority in both malignancy and aggressiveness prediction on the internal validation and combined external test cohorts. **b**, A comprehensive comparison across five key performance metrics in the combined external cohort further confirms RenalCLIP’s robust diagnostic precision. **c**, Bar charts comparing the ROC AUC for malignancy (top) and aggressiveness (bottom) prediction across the five proprietary external cohorts and the public TCIA cohort highlight RenalCLIP’s consistent performance advantage. **d,e**, Representative ROC curves for the internal validation cohort visualize the performance margin for malignancy (**d**) and aggressiveness (**e**) diagnosis. **f,g**, Kaplan-Meier analysis in the challenging TCIA cohort validates the clinical relevance of the aggressiveness prediction, showing significant RFS stratification for patients based on RenalCLIP’s predictions (**f**) but not for those based on the baseline model, CNN (**g**). Hazard ratios (HR) and corresponding p-values shown were derived from a univariate Cox proportional hazards model, while p-values for overall curve comparison were calculated using a two-sided log-rank test. Shaded areas in the survival curves and capped error bars in the bar charts represent 95% confidence intervals, and the centers of the bars correspond to the computed values of each metric.

Moving beyond binary malignancy, we evaluated the model’s performance on the more nuanced task of aggressiveness stratification, which is paramount for personalized treatment selection⁴⁴. Here again, RenalCLIP demonstrated superior accuracy compared to all baseline models in the internal cohort (Fig. 3a). In the combined external test cohort, RenalCLIP achieved leading performance metrics, including an ROC AUC of 0.703, PR AUC of 0.460, sensitivity of 0.713, specificity of 0.613, and an F1-score of 0.506 (Fig. 3b). A detailed cohort-level analysis further underscored its robust generalizability, showing that RenalCLIP consistently outperformed other models across most external cohorts (Fig. 3c and Supplementary Table. 13).

To validate the clinical relevance of this aggressiveness classification, we investigated whether the prediction of the model could stratify patients into distinct prognostic groups, as oncologic outcomes are the ultimate manifestation of tumor aggressiveness. In the internal validation cohort, tumors classified as aggressive by RenalCLIP exhibited significantly worse RFS outcomes compared to those predicted to be indolent ($p=0.005$, $HR=10.5$), a capability shared by most baseline models in this less challenging setting (Extended Data Fig. 4a–e). In stark contrast, within the independent TCIA cohort, only the predictions made by RenalCLIP retained statistically significant prognostic power ($p=0.010$, $HR=2.23$) (Fig. 3f). Notably, tumors stratified by any of the baseline models, including CNN ($p=0.225$, $HR=1.40$), CT-CLIP ($p=0.590$, $HR=1.26$), Merlin ($p=0.178$, $HR=1.44$), and CT-FM ($p=0.094$, $HR=1.64$), showed no significant difference in RFS (Fig. 3g, Extended Data Fig. 4f–h). This unique ability to retain prognostic significance in a challenging external cohort provides powerful, clinically meaningful evidence for the robust generalizability of RenalCLIP’s aggressiveness characterization.

2.4 Non-invasive prognostic biomarker for kidney cancer survival

Accurate prognosis prediction is crucial for guiding personalized follow-up strategies and adjuvant therapy decisions in renal cancer. With a lack of reliable non-invasive biomarkers¹², CT-based indicators offer a promising alternative^{45,46}. We therefore evaluated whether a risk score derived from RenalCLIP could serve as a reliable prognostic biomarker. Initial analysis showed that RenalCLIP achieved the highest Concordance Index (C-index) for predicting RFS across the internal validation cohort (0.864), the combined external test cohort (0.671), and the TCIA cohort (0.726). Acknowledging the limited follow-up periods in some external sites, we focused our subsequent in-depth validation primarily on the TCIA cohort. Within this cohort, RenalCLIP demonstrated a substantial advantage over baseline models: it outperformed the top-performing baseline (CT-FM) by 22.6% for RFS (0.726 vs. 0.592), by 6.3% for disease-specific survival (DSS; 0.690 vs. 0.649), and by 4.3% for overall survival (OS; 0.650 vs. 0.623) (Fig. 4a). We refer the reader to Supplementary Tables 14–16 for more detailed results of model performance.

To assess its clinical utility in risk stratification, we categorized patients into high- and low-risk groups based on the cohort-specific median score. Kaplan-Meier analysis in the TCIA cohort revealed that RenalCLIP provided the most significant and clearest risk stratification for RFS. Patients in the RenalCLIP-defined high-risk group

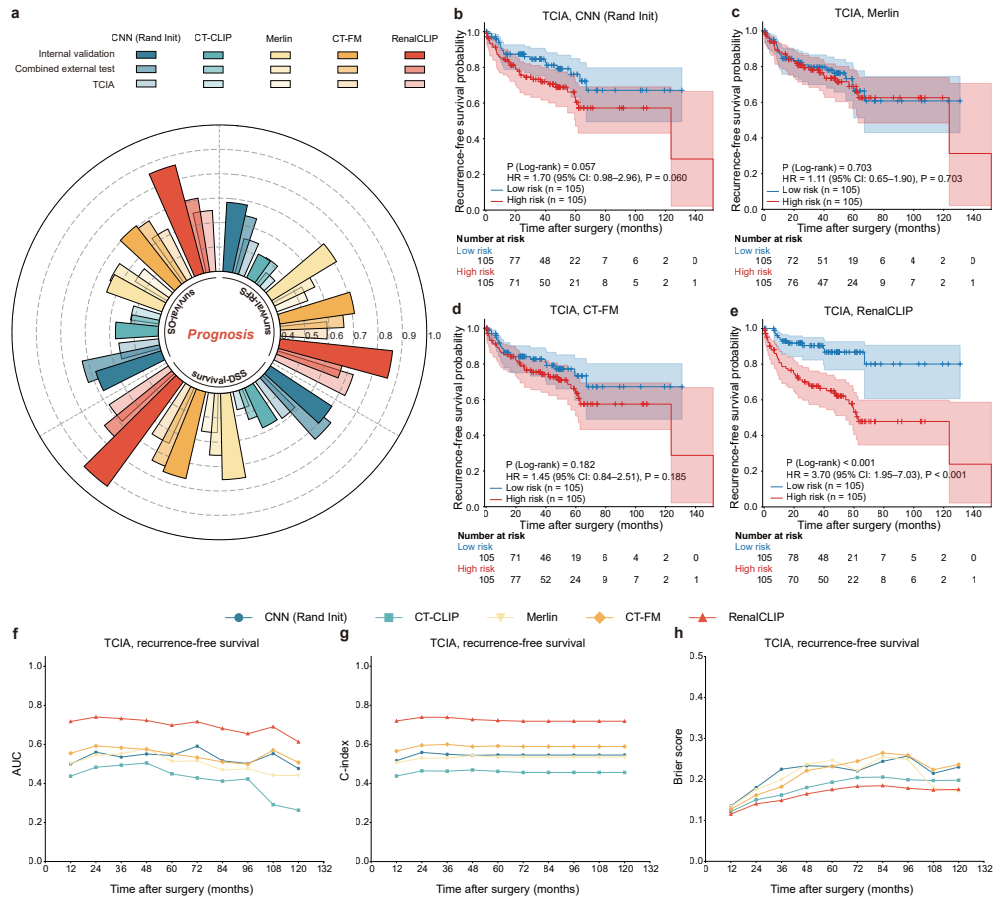


Fig. 4 | Performance of RenalCLIP on prognosis of renal tumors. **a**, Rose plots comparing Harrell’s C-index for recurrence-free survival (RFS), disease-specific survival (DSS), and overall survival (OS) demonstrate the superior prognostic accuracy of RenalCLIP across the internal validation cohort, the combined external test cohort, and the TCIA cohort. **b–e**, Kaplan-Meier analyses for RFS in the TCIA cohort validate the clinical relevance of the derived risk scores. While patient stratification based on risk scores from baseline models including CNN (**b**), Merlin (**c**), and CT-FM (**d**) failed to show statistically significant survival differences, the stratification by RenalCLIP provided clear and significant prognostic separation between high- and low-risk groups (**e**). **f–h**, Time-dependent analyses in the TCIA cohort further confirm RenalCLIP’s durable prognostic power, showing its sustained superiority over baseline models across all evaluated time points as measured by ROC AUC (**f**), C-index (**g**), and Brier score (**h**). Hazard ratios (HR) and corresponding p-values shown on survival curves were derived from a univariate Cox model; p-values for overall curve comparison were from a two-sided log-rank test. Shaded areas in the survival curves (**b–e**) represent 95% confidence intervals.

had significantly worse survival than the low-risk group, exhibiting the highest hazard ratio among all models ($p < 0.001$, $HR = 3.7$) (Fig. 4b–e). Furthermore, RenalCLIP demonstrated strong and statistically significant prognostic power for both DSS and OS (Extended Data Fig. 5a–j). To confirm that this prognostic value was independent of established clinical standards, we next performed multivariate Cox regression analysis. After adjusting for standard pathological indicators such as TNM stage and WHO/ISUP grade, the RenalCLIP risk score remained an independent adverse prognostic factor for RFS in the TCIA cohort ($p = 0.016$, $HR = 2.27$), while the risk scores derived from all baseline models failed to retain statistical significance (see Supplementary Tables 17–18 for details).

Furthermore, we performed time-dependent analyses to evaluate the stability of the model’s predictive accuracy over time. For RFS, RenalCLIP consistently outperformed all baseline models at all evaluated time points, as measured by ROC AUC (Fig. 4f), C-index (Fig. 4g), and Brier score for prediction error (Fig. 4h). Similar superiority was observed for DSS and OS across the same time range (Extended Data Fig. 6a–f).

Collectively, these comprehensive analyses establish RenalCLIP as a robust and independent prognostic biomarker. Its ability to non-invasively predict patient outcomes from pre-operative imaging offers significant potential to refine clinical trial enrichment, guide personalized management, and improve patient counseling.

2.5 Zero-shot generalization and data efficiency

A critical barrier to the widespread clinical deployment of deep learning models is their heavy reliance on large, expert-annotated datasets, which are scarce and labor-intensive to create^{47,48}. To overcome this, we designed RenalCLIP to excel in low-data regimes. We rigorously evaluated two of its hallmark capabilities: first, its ability to generalize to novel tasks via zero-shot transfer without any fine-tuning³³, and second, its data efficiency when adapted to new tasks with limited labeled samples.

To quantitatively validate the quality of the shared embedding space learned by RenalCLIP, we assessed its cross-modal retrieval performance. This task serves as a direct probe of the model’s vision-language alignment and has practical applications in cohort identification and medical education. We benchmarked RenalCLIP against other vision-language models (CT-CLIP and Merlin) using Recall@K ($K = 1, 3, 5$) on five cohorts containing radiology reports. RenalCLIP substantially outperformed both baselines across all cohorts in both text-to-image (t2i) and image-to-text (i2t) retrieval (Fig. 5a and Supplementary Tables 19–23). For instance, in the t2i task, RenalCLIP achieved a mean Recall@5 of 0.120 across the five cohorts, representing a stark improvement over Merlin (0.051) and CT-CLIP (0.004).

Building on this strong cross-modal alignment, we next evaluated the model’s zero-shot classification performance on malignancy and aggressiveness diagnosis. To ensure a robust evaluation against linguistic variations, we employed a prompt ensemble methodology and assessed performance under two distinct strategies: a deterministic approach using maximum similarity and a stochastic prompt sampling strategy (see Supplementary Tables 24–26 for prompts used for each class in zero-shot classification and Methods for details). Our results show that RenalCLIP is robust to the choice

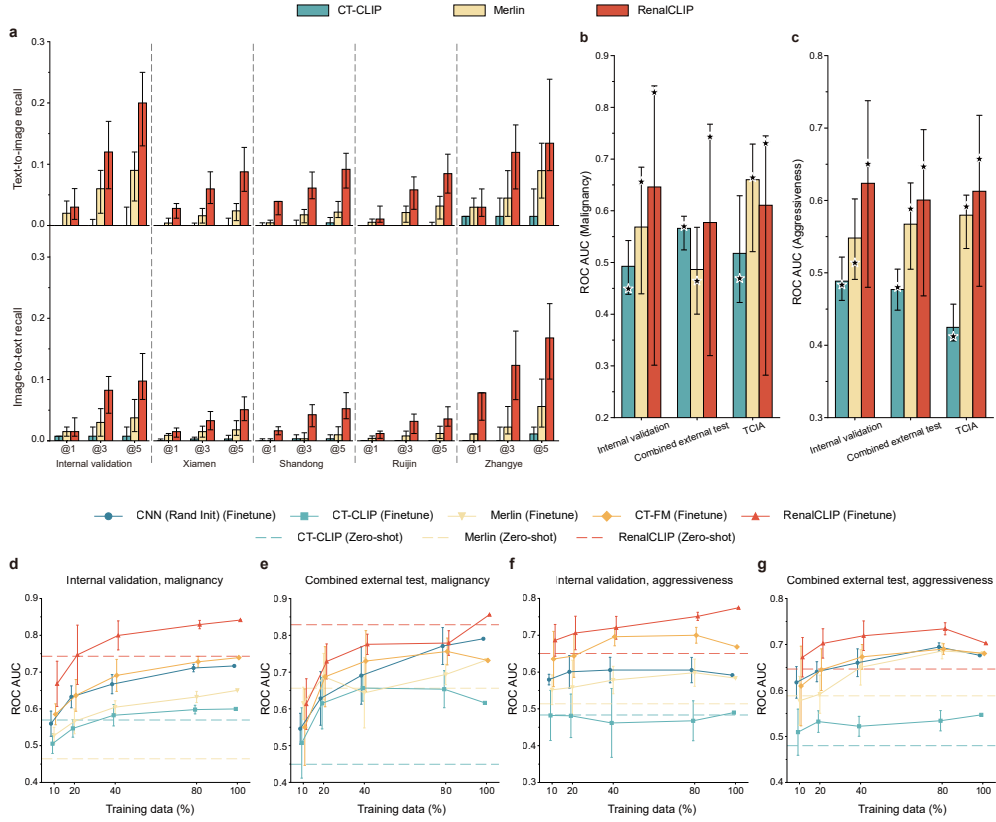


Fig. 5 | Performance of RenalCLIP on zero-shot transfer and data-efficient fine-tuning. **a**, Cross-modal retrieval performance on five cohorts, quantified by Recall@K (K=1, 3, 5). The plots for text-to-image (t2i, top) and image-to-text (i2t, bottom) retrieval show that RenalCLIP substantially outperforms other vision-language models. **b,c**, Zero-shot classification performance for malignancy (**b**) and aggressiveness (**c**) prediction on three test cohorts. Bar plots show the mean ROC AUC from a stochastic prompt sampling strategy, while star markers indicate the performance using a deterministic maximum similarity strategy. **d–g**, Data-efficient fine-tuning performance on the internal (**d,f**) and combined external (**e,g**) cohorts for malignancy (**d,e**) and aggressiveness (**f,g**) prediction. The plots show model ROC AUC as a function of the fraction of training data used for fine-tuning. Dashed horizontal lines indicate the zero-shot performance of each model for reference. The results highlight both RenalCLIP’s high data efficiency (achieving strong performance with only 20–40% of data) and the power of its pre-training, as its zero-shot performance frequently surpasses the fully fine-tuned performance of baseline models. In panels **b** and **c**, the centers of the bars correspond to the average ROC AUC from 1,000 bootstrap samples, and error bars represent 95% confidence intervals. In panels **d–g**, data points for training fractions less than 100% represent the mean ROC AUC from five random sampling runs, with capped error bars indicating the standard deviation; the 100% data point represents a single run.

of evaluation strategy and consistently outperforms baseline models. Using the primary maximum similarity ensemble strategy, RenalCLIP substantially outperformed all baselines on both tasks across all three test cohorts (Fig. 5b–c and Supplementary Tables 27–28). On the challenging TCIA cohort, for example, RenalCLIP achieved an ROC AUC of 0.730 for malignancy prediction, significantly outperforming Merlin (0.664) and CT-CLIP (0.605). A similar margin of superiority was observed for aggressiveness prediction, where RenalCLIP (AUC=0.657) again surpassed both Merlin (0.591) and CT-CLIP (0.412).

Finally, we investigated the value of RenalCLIP’s pre-trained features for downstream data efficiency. When fine-tuned, RenalCLIP demonstrated remarkable data efficiency, achieving performance comparable to fully-trained baseline models while using only 20–40% of the labeled images on both malignancy and aggressiveness tasks (Fig. 5d–g). The power of its pre-trained representations was most strikingly evident when comparing its zero-shot performance directly against fine-tuned models. For malignancy prediction, RenalCLIP’s zero-shot model surpassed the peak performance of all baseline models—even after they were fully fine-tuned on 100% of the data—across both internal and combined external cohorts. When compared against itself on the external cohort, its zero-shot generalization was so effective that it outperformed the RenalCLIP model fine-tuned on up to 80% of the data and was comparable to the fully fine-tuned version (Fig. 5d–e). For the more challenging aggressiveness task, although fine-tuning on RenalCLIP improved performance over its zero-shot baseline (even with only 10% of the data), this zero-shot performance itself remained highly competitive against the other fine-tuned models; it exceeded the peak fine-tuned results of the CNN, CT-CLIP, and Merlin models in the internal cohort, and its performance in the external cohort was comparable to that of the CNN, Merlin, and CT-FM models when fine-tuned on 40% of the data (Fig. 5f–g). The detailed analysis for the TCIA cohort, which showed similar trends of strong zero-shot performance, is provided in Extended Data Fig. 7. We refer readers to Supplementary Tables 29–30 for more detailed reporting of model performance.

3 Discussion

In this study, we developed and validated RenalCLIP, a disease-centric vision-language foundation model that establishes a new paradigm for the comprehensive, non-invasive assessment of renal masses from CT imaging. By uniquely integrating deep visual features with the rich semantic context of radiological reports through a novel knowledge-enhancement strategy, RenalCLIP demonstrates superior performance, generalizability, and data efficiency across a wide spectrum of clinical tasks compared to both conventional AI models³⁴ and existing general-purpose CT foundation models^{35–37}.

The management of renal masses presents a cascade of clinical challenges where precision is paramount: the non-invasive differentiation of benign from malignant tumors to prevent overtreatment, the stratification of tumor aggressiveness to guide risk-adapted therapies like active surveillance, and the accurate prediction of postoperative prognosis to personalize follow-up and adjuvant treatment decisions. Current

imaging interpretation struggles to meet these needs, and the utility of percutaneous biopsy is limited by significant non-diagnostic rates and potential complications.

Aiming to address these challenges, prior AI research has largely focused on radiomics and conventional deep learning. For instance, in malignancy diagnosis, one of the largest CT-based radiomics models achieved an AUC of 0.75 in a cohort of 735 patients⁴⁹. Similarly, for aggressiveness assessment, a notable radiomics signature developed to distinguish low-grade from high-grade clear cell renal cell carcinoma (RCC) reached an AUC of 0.70 in 587 patients⁵⁰. However, the clinical translation of such models has been consistently hampered by a narrow single-task focus, small cohort sizes, and a frequent lack of independent external validation; indeed, in the few studies where external validation was performed, these models often exhibited poor generalizability. More recent general CT foundation models, while powerful, lack the disease-centric focus required for high-stakes, nuanced clinical questions in oncology. Although models like CT-FM and Merlin demonstrate versatility in broad tasks such as whole-body segmentation, and CT-CLIP excels in chest imaging, their pre-training corpora are not enriched with sufficient, high-quality examples of renal cancer. Our head-to-head comparisons confirmed this limitation: their performance on fine-grained tasks like aggressiveness prediction and prognostication was significantly inferior to RenalCLIP.

In contrast, RenalCLIP is explicitly designed to fill this gap by integrating deep visual features with renal-specific clinical-pathological semantics. This disease-centric design, which infuses the model with specialized knowledge through a unique pre-training strategy, enables RenalCLIP to excel in nuanced oncology tasks. It offers a level of precision in aggressiveness stratification and prognostication that general-purpose foundation models, which lack this targeted training, cannot match.

A key advantage of RenalCLIP is its robust generalizability, which we attribute to our disease-centric strategy coupled with the large scale of our multi-center pre-training dataset. It was demonstrated through three key findings. First, the performance gap between RenalCLIP and baseline models widened substantially in external cohorts. For malignancy diagnosis, RenalCLIP’s margin over the top CNN baseline expanded from 8.2% in the internal cohort to 17.3% in the combined external validation, underscoring its robustness against domain shifts. Second, while predictions from both RenalCLIP and most baseline models could significantly stratify patient RFS in the internal validation cohort, only those from RenalCLIP retained this statistically significant prognostic capability in the independent TCIA cohort, where all baselines failed. Finally, despite being pre-trained predominantly on data from a Chinese population, RenalCLIP demonstrated strong cross-ethnic validity by consistently outperforming all baseline models across all tasks in the primarily Caucasian TCIA cohort.

Beyond its robust generalizability, the power of RenalCLIP’s pre-trained representations was most evident in its remarkable data-efficient learning capability, which addresses a fundamental barrier to the translation of AI in medicine: the scarcity of large, expert-annotated datasets. Its zero-shot performance in malignancy prediction was particularly striking, surpassing the peak performance of fully fine-tuned baseline models. This is not merely a technical achievement; it signifies a potential paradigm

shift in how specialized medical AI tools are developed. This capability opens a feasible pathway for rapidly extending the model to other critical but data-scarce problems in renal oncology. For instance, developing classifiers for rare but aggressive histologic subtypes (e.g., collecting duct carcinoma, medullary carcinoma), predicting response to targeted therapies, or identifying genomic markers from imaging currently suffers from a lack of sufficient training examples. The strong few-shot and zero-shot performance of RenalCLIP suggests it could serve as a powerful foundational platform to tackle these "long-tail" clinical challenges with minimal data requirements.

Finally, the clinical value of these advanced capabilities was crystallized in the validation on meaningful prognostic endpoints. For aggressiveness stratification, many models, including our baselines, could separate prognostic groups in the less challenging internal cohort. However, the true test of generalizability came from the independent TCIA cohort, where only RenalCLIP's predictions retained statistically significant prognostic power. This finding has profound clinical implications. A reliable, non-invasive biomarker for aggressiveness, available at the time of initial diagnosis, could fundamentally alter patient management by enabling more confident use of active surveillance for low-risk tumors, guiding decisions on adjuvant therapy trials for high-risk patients post-nephrectomy, and improving patient counseling.

Despite these promising results, our study has several limitations that must be acknowledged. First, the analysis was retrospective, which may introduce selection and spectrum biases; prospective validation in a real-world clinical workflow is essential to confirm its utility. Second, while validated on the multi-ethnic TCIA cohort, our pre-training data was predominantly from a Chinese population. Given the known ethnic variations in renal cancer incidence and biology, further training and validation on more diverse global populations, particularly from African and Hispanic ancestries, are warranted. Third, while RenalCLIP's report generation was superior to baselines, it is not yet at human-expert-level and can still exhibit minor factual inconsistencies, highlighting that high-fidelity medical report generation remains a significant challenge. Finally, our evaluation, while comprehensive, did not extend to predicting genomic profiles (e.g., BAP1, PBRM1 mutations) from imaging, which is a critical frontier in radiogenomics and an important avenue for future work.

In conclusion, RenalCLIP provides a robust, multi-task foundation for renal cancer assessment that bridges the gap between radiological imaging and clinical semantics. This work establishes the necessity and effectiveness of a disease-centric pre-training strategy for building high-performing, generalizable, and trustworthy medical foundation models. This disease-centric paradigm serves as a blueprint for developing similar specialized AI systems in other areas of oncology, potentially accelerating the integration of artificial intelligence into the core of personalized patient care.

4 Methods

4.1 Study cohorts and data preprocessing

4.1.1 Study population

This retrospective study was approved by the institutional review boards of all participating medical centers and complied with all relevant ethical regulations, in accordance with the Declaration of Helsinki. The requirement for written informed consent was waived by the ethics committees due to the retrospective nature of the analysis, which involved pre-existing anonymized CT images and posed no additional risk to the patients. We screened patients who underwent nephrectomy or biopsy for suspicious renal masses between January 1, 2009, and October 30, 2023, from ten medical centers in China and the public Cancer Imaging Archive (TCIA). The key inclusion criterion was the availability of preoperative multi-phase CT scans. Patients were excluded if they had received neoadjuvant therapy, had a diagnosis of hereditary renal cell carcinoma (RCC), or if their CT scans exhibited severe artifacts. This screening process yielded a final study population of 8,809 patients providing a total of 27,866 preoperative CT scans, which were subsequently divided into pre-training and downstream task datasets.

The pre-training dataset was sourced from four major medical centers (Zhongshan Hospital of Fudan University, The First Affiliated Hospital of Zhejiang University, Qilu Hospital of Shandong University, and Linyi City People’s Hospital) and comprised a total of 6,867 patients (21,819 CT scans). This dataset was further partitioned into a training set of 6,367 patients (20,278 scans) and a validation set of 500 patients (1,541 scans). The validation set was used exclusively for selecting the best-performing model checkpoint during the pre-training phase.

The downstream task dataset, used for fine-tuning and evaluation, consisted of a separate cohort of 1,942 patients (6,047 CT scans). This included an internal cohort sourced from the pre-training institutions, with the exception of Linyi City People’s Hospital, which was partitioned into a training set of 400 patients (1,240 scans) and a validation set of 100 patients (316 scans). For comprehensive external validation, we assembled five proprietary cohorts from the following institutions: Xiamen Branch of Zhongshan Hospital (termed the Xiamen cohort; 251 patients, 796 scans), Shandong Cancer Hospital & Institute (termed the Shandong cohort; 250 patients, 991 scans), Ruijin North Hospital of Shanghai Jiao Tong University (termed the Ruijin cohort; 229 patients, 727 scans), The First People’s Hospital of Lianyungang (termed the Lianyun cohort; 220 patients, 671 scans), and Zhangye People’s Hospital of Hexi University (termed the Zhangye cohort; 67 patients, 259 scans). These five cohorts were aggregated to form the combined external test cohort used for pooled analyses. The public TCIA cohort (425 patients, 1,047 scans) was used as an additional, independent validation set.

Radiologic reports were unavailable for the Lianyun and TCIA cohorts, while such reports were accessible for all other cohorts. The detailed clinicopathological characteristics of all cohorts are provided in Extended Data Table 1.

4.1.2 Histologic classification

Renal tumors were classified into three categories—benign indolent, malignant indolent, and malignant aggressive—based on previous research^{4,51}. Benign indolent renal masses included angiomyolipoma, complex renal cyst, oncocytoma, mixed epithelial and stromal tumor, metanephric adenoma, among others. Malignant indolent renal tumors encompassed indolent clear cell renal cell carcinoma (ccRCC, defined as ccRCC without invasion into major veins or perinephric tissues, grade 3–4 components, necrosis, or sarcomatoid differentiation), indolent papillary RCC (papillary RCC without invasion into major veins or perinephric tissues, grade 3–4 components, or sarcomatoid differentiation), chromophobe RCC, clear cell papillary renal cell tumors, multilocular cystic renal neoplasm of low malignant potential, epithelioid angiomyolipoma, and others. Malignant aggressive subtypes included aggressive ccRCC (non-indolent ccRCC), aggressive papillary RCC (non-indolent papillary RCC), TFE3-rearranged renal cell carcinoma, renal cell carcinoma NOS, and other high-risk variants. Tumor stage at the time of surgery was determined according to the 8th edition of the AJCC cancer staging system. For cases with available slides, three pathologists re-evaluated tumor subtypes in accordance with the 2022 WHO classification for renal tumors and tumor nuclear grades based on the WHO/ISUP grading system for cases with available slides. The detailed distribution of these histologic subtypes and tumor grades for the entire cohort is provided in Extended Data Table 1.

4.1.3 CT image acquisition and preprocessing

To ensure spatial correspondence across the multi-phase CT scans (non-contrast (N), arterial (A), venous (V), and delayed (D)), all available phases for a given patient were aligned to the coordinate system of the arterial phase by resampling them onto its grid. If the arterial phase was unavailable, the venous phase was used as the reference (all scans in the study included at least one contrast-enhanced phase). This process was performed using the BRAINSResample module within 3D Slicer (v4.11.20210226) with linear interpolation.

Following this alignment, we employed a semi-automated pipeline to localize the region of interest (ROI) (Extended Data Fig. 1a). A pre-trained nnU-Net⁵² model was first utilized to automatically segment the kidneys, renal cysts, and tumors. The subsequent localization strategy differed by task. This distinction was intentional, reflecting the different objectives of each stage: the pre-training phase was designed to maximize data diversity and learn robust features from the entire kidney, where precise lesion-centric localization was less critical, whereas the downstream tasks required highly accurate ROI definition centered on the lesion to learn task-specific diagnostic features. For the pre-training dataset, the ROI was automatically defined as the geometric center of the segmented foreground; in the rare event that the segmentation model produced no foreground mask, the kidney center was then manually annotated with a single point by an expert radiologist. For the downstream task datasets, an initial ROI center was proposed by identifying the axial slice with the largest cross-sectional area of the primary lesion (tumors prioritized over cysts) and calculating the lesion’s geometric center on that slice. To ensure localization accuracy, an expert

radiologist reviewed the quality of the underlying nnU-Net segmentations. The automatically calculated center point was used for all accurately segmented lesions. In cases of poor segmentation, the radiologist instead manually placed a single point to define the lesion center. All manual point annotations were performed using 3D Slicer.

Following the established protocol^{51,53}, a 3D volume centered on the localized ROI was cropped to a fixed physical size of $140 \times 140 \times 160$ mm. These volumes were then resampled to an anisotropic spacing of $1.0 \times 1.0 \times 5.0$ mm, yielding a uniform input size of $140 \times 140 \times 32$ voxels. Finally, image intensities were normalized by windowing with a window level of 50 Hounsfield Units (HU) and a window width of 500 HU.

The strategy for selecting input volumes also varied by task. For pre-training, cropped volumes from both kidneys of each patient were utilized. For downstream tasks, only the kidney containing the primary lesion was included; in cases with bilateral lesions, the lesion determined to be most aggressive via pathology reports was selected. During model training, a $128 \times 128 \times 32$ voxel patch was randomly cropped from the larger $140 \times 140 \times 32$ volume for data augmentation. During inference, a deterministic center crop of the same size was used.

For all comparison models, we utilized their officially provided preprocessing functions and default configurations. The input for these models was based on the same lesion-centered ROIs generated by our pipeline to ensure a fair comparison.

4.1.4 Radiology report processing

The original free-text radiology reports, sourced in Mandarin Chinese, underwent a two-step processing pipeline to align with the single-kidney image inputs. First, given that our image encoder processes individual kidneys, we developed a large language model (LLM)-based method⁴⁰ to parse each report and partition the descriptive text into ‘left kidney’ and ‘right kidney’ components. Second, following this anatomical separation, the partitioned Chinese texts were programmatically translated into English to facilitate model development (Extended Data Fig. 1b). The specific prompts designed for both the report partitioning and translation tasks are detailed in the Supplementary Tables 31–32.

4.2 Multi-phase CT data handling and fusion strategy

Our core strategy for handling multi-phase CT scans treats each available phase from a patient’s scan as an independent 3D sample. This approach serves two primary objectives: first, to substantially augment the effective size of our training dataset, and second, to implicitly regularize the model by exposing it to a wide variety of imaging contexts.

During the pre-training stage, our data loader randomly samples a single, existing phase for each patient within a batch. This forces the model to learn a robust feature representation that is agnostic to the specific enhancement characteristics of any single phase. For the primary downstream validation experiments, however, we adopted a standardized single-phase input to ensure fair comparison against baseline models, which typically utilize a single 3D volume (Extended Data Fig. 9a). Specifically, we prioritized the arterial phase, followed by the venous phase if the former was

unavailable. This hierarchy reflects established clinical practice, as the arterial phase optimally demonstrates tumor vascularity and the venous phase is crucial for assessing both tumor margin and contrast washout patterns.

Finally, to quantify the performance benefit of integrating multi-phase information, we conducted an ablation study. For this study, a model was first fine-tuned on the downstream tasks using a random single-phase sampling strategy, analogous to the method used in pre-training stage. At inference time, this trained model was then evaluated using a late-fusion approach: each of a patient’s available 3D phase volumes was independently passed through the model to generate phase-specific logits. These logits were then combined via element-wise averaging to produce a single, fused prediction.

4.3 RenalCLIP pre-training

RenalCLIP is a self-supervised learning model specifically designed for the RCC CT imaging domain. It builds upon the success of established language-image pre-training (e.g., CLIP³³) in the natural image domain. RenalCLIP integrates two core components: an image encoder $f(\cdot; \theta_f)$ and a text encoder $g(\cdot; \theta_g)$. The image encoder $f(\cdot; \theta_f)$ is composed of a backbone $f_{\text{backbone}}(\cdot)$, specifically a 3D ResNet18³⁴ adapted for volumetric CT data, and a projection head $f_{\text{proj}}(\cdot)$, where θ_f collectively denotes the parameters of both modules. The projection head maps the high-dimensional features extracted by the image backbone directly to a single global image representation, specifically designed with the same dimensionality as the text features to enable cross-modal alignment through contrastive learning. The text encoder $g(\cdot; \theta_g)$ is built upon the Llama3 8B architecture³⁰ and leverages LLM2Vec³¹ technology. It comprises 32 transformer layers, featuring an embedding dimension of 4,096 and a hidden dimension of 14,336. A global representation of each caption is extracted by taking the mean of the last_hidden_state outputs across all its tokens. The text encoder does not employ an additional projection head and remains frozen during this phase, motivated by recent evidence^{54,55} that text embeddings from a fixed pre-trained text encoder are highly effective for guiding visual representation learning.

4.3.1 Uni-modal pre-training via knowledge enhancement

Previous research^{22,56} suggests that sequentially pre-training uni-modal modules prior to joint visual-language pre-training, significantly improves zero-shot transfer performance. Following this strategy, both our image and text encoders undergo independent pre-training.

Image encoder pre-training

We pre-trained the image encoder using a multi-task learning approach, leveraging structured labels derived from original radiology reports. Clinical experts designed 14 critical questions, each with several options, focusing on key aspects relevant to kidney cancer imaging interpretation. An LLM (GPT-4o⁴⁰) then parsed the free-text reports based on these question-option pairs to extract the required structured attributes, capturing the semantic hierarchy. These extracted results were converted

into a one-hot encoding format for model training. The image backbone was pre-trained by minimizing a classification loss (categorical cross-entropy), defined as:

$$\mathcal{L}_{\text{CLS}} = - \sum_{i=1}^N \sum_{j=1}^C \mathbf{1}[y^{(i)} = j] \log(\hat{y}_j^{(i)}) \quad (1)$$

where N denotes the number of samples, and C represents the number of classes for each question. $\mathbf{1}[\cdot]$ is the indicator function, which equals 1 if the specified condition is satisfied and 0 otherwise. $y^{(i)}$ is the ground truth label of the i -th sample, and $\hat{y}_j^{(i)}$ denotes the predicted probability that sample i belongs to class j . This process was crucial for injecting domain-specific clinical knowledge into the image encoder, enhancing its ability to capture features vital for RCC diagnosis and characterization from CT images. Specific questions, options, and prompts for structured attribute extraction are in Supplementary Tables 33–35.

Text encoder pre-training

Our text encoder is built upon the Llama3 8B architecture and leverages LLM2Vec technology, which transforms state-of-the-art LLMs into potent text feature extractors. Its core methodology involves three key steps: first, replacing the LLM’s causal attention mechanism with a bidirectional structure to enhance contextual semantic understanding. Second, masked language modeling^{57,58} (MLM) is applied. In this unsupervised framework, parts of words in reports are masked, and the model is trained to predict their original identity based on their bidirectional context, thereby capturing rich contextual representations. This step fine-tunes the LLM using LoRA⁵⁹ (Low-Rank Adaptation) on the MIMIC-CXR dataset⁶⁰ (227,973 chest X-ray reports) to significantly improve general medical domain comprehension. The MLM loss is formulated as:

$$\mathcal{L}_{\text{MLM}} = - \frac{1}{N} \frac{1}{M} \sum_{i=1}^N \sum_{\mathbf{t} \in \mathcal{M}} \sum_{v=1}^V \mathbf{1}[y_{\mathbf{t}} = v] \log(\hat{p}_v^{(\mathbf{t})}) \quad (2)$$

where N denotes the number of samples, \mathcal{M} represents the set of masked tokens, M is the number of elements in \mathcal{M} , V is the vocabulary size, $y_{\mathbf{t}}$ is the ground truth label for token \mathbf{t} , and $\hat{p}_v^{(\mathbf{t})}$ denotes the predicted probability that token \mathbf{t} corresponds to the v -th vocabulary item. Third, contrastive learning with SimCSE⁶¹ further refines the text encoder’s understanding of kidney cancer-related terminology. Here, an input sentence is passed twice through the model with independently sampled dropout masks to generate representations \mathbf{h}_i and its distinct positive representations \mathbf{h}_i^+ , which are then maximized in similarity, while simultaneously minimizing their similarity with negative samples (representations of other sentences in the batch). This SimCSE objective function is formulated as follows:

$$\mathcal{L}_{\text{SimCSE}} = - \frac{1}{N} \sum_{i=1}^N \log \left(\frac{\exp(\text{sim}(\mathbf{h}_i, \mathbf{h}_i^+)/\tau)}{\sum_{j=1}^N \mathbf{1}[j \neq i] \exp(\text{sim}(\mathbf{h}_i, \mathbf{h}_j)/\tau)} \right) \quad (3)$$

where N is the number of samples in a mini-batch, τ is a temperature hyperparameter, and $\text{sim}(\mathbf{h}_i, \mathbf{h}_j)$ denotes the cosine similarity between \mathbf{h}_i and \mathbf{h}_j , which is defined as:

$$\text{sim}(\mathbf{h}_i, \mathbf{h}_j) = \frac{\mathbf{h}_i^\top \mathbf{h}_j}{\|\mathbf{h}_i\| \|\mathbf{h}_j\|} \quad (4)$$

where $\|\mathbf{h}_i\|$ and $\|\mathbf{h}_j\|$ denote the L2 norms of \mathbf{h}_i and \mathbf{h}_j , respectively. This fine-tuning is also conducted using LoRA and is applied to the training set of our internal pre-training dataset.

4.3.2 Cross-modal visual-language pre-training

Following uni-modal pre-training, RenalCLIP undergoes cross-modal visual-language pre-training³³. A mini-batch is constructed from N image-report pairs, denoted as $(\mathbf{x}_i, \mathbf{r}_i)_{i=1}^N$, where \mathbf{x}_i is the i -th CT volume and \mathbf{r}_i is a sequence of T word tokens representing its corresponding radiological report. For each pair $(\mathbf{x}_i, \mathbf{r}_i)$, the L2-normalized image representation \mathbf{u}_i is obtained from the cascaded backbone and projection head of the image encoder $f(\cdot; \theta_f)$, and the L2-normalized report representation \mathbf{v}_i is derived from the text encoder $g(\cdot; \theta_g)$.

The model is trained to align positive (matching) image-report pairs and push apart negative (non-matching) pairs within the shared embedding space using a symmetric InfoNCE loss. The complete objective is given by:

$$\mathcal{L}_{\text{CLIP}} = -\frac{1}{N} \sum_{i=1}^N \left(\log \frac{\exp(\text{sim}(\mathbf{u}_i, \mathbf{v}_i)/\tau)}{\sum_{k=1}^N \exp(\text{sim}(\mathbf{u}_i, \mathbf{v}_k)/\tau)} + \log \frac{\exp(\text{sim}(\mathbf{u}_i, \mathbf{v}_i)/\tau)}{\sum_{k=1}^N \exp(\text{sim}(\mathbf{u}_k, \mathbf{v}_i)/\tau)} \right) \quad (5)$$

where $\text{sim}(\mathbf{u}, \mathbf{v})$ denotes the cosine similarity between representations \mathbf{u} and \mathbf{v} , and τ is a learnable temperature parameter that scales the similarity scores. This dual-sided objective ensures that both image-to-text and text-to-image alignments are optimized simultaneously, driving the model to learn semantically rich and aligned representations for renal CT volumes and their corresponding reports.

4.3.3 Pre-training configuration

Our uni-modal pre-training involved separate stages for the image backbone and the text encoder. The image backbone was pre-trained using an AdamW optimizer⁶² on a single NVIDIA A100 80GB GPU. Training spanned up to 200 epochs with a batch size of 300 and a learning rate of 5×10^{-4} . After each epoch, the model’s performance was validated on the pre-training validation set, and the best-performing model checkpoint was saved based on the highest macro-averaged AUC across 14 key attributes, reflecting its strong multi-task learning capabilities. The text encoder pre-training, utilizing LLM2Vec, consisted of two sequential steps, both optimized with AdamW on a single NVIDIA A100 80GB GPU. To reduce computational overhead, both steps incorporated gradient checkpointing⁶³ and mixed-precision training (bfloat16). Each

step was trained for 1,000 iterations with a batch size of 32. The initial phase, leveraging MLM, used a learning rate of 5×10^{-5} and an MLM probability of 0.2. This was followed by the SimCSE phase, which employed a learning rate of 3×10^{-5} and a SimCSE dropout rate of 0.2. Detailed hyperparameters for uni-modal pre-training are provided in Supplementary Tables 36–38.

Our visual-language pre-training experiments were conducted on four NVIDIA A100 80GB GPUs, utilizing a local batch size of 1,024 per GPU and mixed-precision training (bfloat16) for enhanced efficiency. We employed AdamW as the optimizer. The image encoder’s backbone was trained with an initial learning rate of 1×10^{-5} , while its projection head used 5×10^{-4} . The model was trained for 100 epochs, incorporating a 10-epoch warmup phase. Following each training epoch, we evaluated cross-modality retrieval performance on the pre-training validation set. The checkpoint demonstrating the best retrieval performance was selected as the final model weights. For more detailed cross-modal pre-training hyperparameter configurations, please refer to Supplementary Table 39.

For image data, augmentation strategies included random crop, random affine transformations, and variations in signal intensity. For more details about data augmentation techniques for 3D CT volumes, please refer to Supplementary Table 40. Regarding text data, features derived from the frozen text encoder were pre-computed and saved offline to disk to minimize computational overhead during training. For text data augmentation, we used sentence shuffling: for each original radiological report, we generated and saved four shuffled versions alongside the original.

4.4 Evaluation of downstream tasks

4.4.1 Baseline models and comparisons

We benchmarked RenalCLIP against a set of state-of-the-art baseline models. The specific models used for comparison varied by the downstream task, reflecting a comprehensive evaluation against both vision-only architectures and vision-language models (VLMs).

For end-to-end fine-tuning on characterization, diagnosis, and prognosis tasks, we included four 3D models. A standard 3D ResNet-18³⁴, trained from scratch with random weight initialization (CNN (Rand Init)), served as the primary image-only baseline. We also included CT-FM³⁷, a 3D vision-only foundation model with a SegResNet⁶⁴ backbone, which was pre-trained on 148,000 whole-body CT scans from the Imaging Data Commons. The set of baselines was completed with two 3D VLMs: CT-CLIP³⁵, a 3D VLM that pairs a Vision Transformer⁶⁵ encoder with a text encoder and was pre-trained on over 50,000 chest CTs, and Merlin³⁶, a 3D VLM designed for abdominal imaging that was pre-trained on approximately 15,000 abdominal CTs paired with EHR data and reports.

For zero-shot cross-modal retrieval and classification, comparisons were limited to the VLMs CT-CLIP and Merlin, as these tasks require pre-trained, paired image and text encoders. The vision-only 3D CNN and CT-FM models were not applicable for these evaluations.

For the image-to-text report generation task, we selected four established models to serve as robust baselines. RadFM⁴² is a VLM specifically designed for medical report generation, pre-trained on a large-scale multi-modal medical dataset of 16 million medical scans with paired text. CT-CHAT³⁵ is another specialized VLM that combines the CT-CLIP vision encoder with a Llama 3.1 8B model, fine-tuned on over 2.7 million question-answer pairs from chest CTs. Additionally, we included two leading 2D VLMs: OpenAI’s GPT-4o⁴⁰, a general-purpose multi-modal model, and Google’s MedGemma⁴¹, a healthcare-specialized model. For these 2D models, the center axial slice of each 3D CT volume was used as the image input.

4.4.2 Evaluation metrics

For the renal mass characterization task (i.e., the five R.E.N.A.L. score components), which are multi-class (three-class) classification tasks, we primarily recorded the Area Under the Receiver Operating Characteristic curve (AUROC). For this, we calculated the macro-averaged AUROC by treating each class as a positive against the others and then averaging the results. For the binary-class diagnosis tasks (malignancy and aggressiveness), a more comprehensive set of metrics was used: AUROC, Precision-Recall Area Under the Curve (PRAUC), sensitivity, specificity, and the F1-score. For these threshold-dependent metrics, the optimal classification threshold for each cohort was determined by maximizing Youden’s J statistic. For prognosis tasks, we used Harrell’s concordance index (C-index) to evaluate how well a model’s predicted risk aligned with the actual order of events. We also employed time-dependent AUROC, C-index, and the Brier score to assess predictive accuracy at various follow-up times. The Brier score specifically measures the accuracy of probabilistic predictions, with lower scores indicating better calibration. For zero-shot and retrieval tasks, we used AUROC for zero-shot classification and Recall@K (with K=1, 3, 5) for retrieval, which measures whether a correct item is found among the top K retrieved results. For the report generation task, we reported BLEU, METEOR, and ROUGE-L scores. These metrics are widely used to evaluate the quality of generated text by comparing n-gram overlap (BLEU-1, BLEU-2, BLEU-4), semantic similarity (METEOR), and the longest common subsequence (ROUGE-L) against human-written reference captions.

4.4.3 Fine-tuning for clinical tasks

To evaluate RenalCLIP’s utility in key renal cancer clinical applications, we fine-tuned the model on various downstream tasks related to RCC characterization, diagnosis, and prognosis. These experiments were conducted using our internal downstream dataset, comprising 400 training samples and 100 validation samples. Model performance was subsequently validated on independent external and TCIA cohorts. The AdamW optimizer was consistently employed, and each model was trained for 100 epochs on a single A100 80GB GPU.

Optimal hyperparameters (learning rate and batch size) for each model and task were determined through a comprehensive grid search. The best-performing model for each comparison was identified based on its performance on the internal validation set: macro-averaged AUC for characterization and diagnosis tasks (specifically macro-AUC for multi-class classification), and c-index for prognosis tasks. These hyperparameter

sets were then used to evaluate the models on the external and TCIA cohorts. Due to variations in GPU memory footprint and model architecture, the hyperparameter search ranges differed across models. For 3D ResNet18 (randomly initialized) and RenalCLIP’s backbone (35,087,424 parameters), batch sizes were searched from [50, 100, 150], and learning rates from $[5 \times 10^{-4}, 1 \times 10^{-4}, 5 \times 10^{-5}, 1 \times 10^{-5}]$. CT-CLIP (176,885,144 parameters) used a fixed batch size of 8, with its learning rate mirroring that of Merlin due to their comparable parameter counts. Merlin (121,882,204 parameters) used a fixed batch size of 16, and its learning rates were searched from $[1 \times 10^{-4}, 5 \times 10^{-5}, 1 \times 10^{-5}]$. For CT-FM (77,760,992 parameters), batch sizes were searched from [50, 100], and learning rates from $[5 \times 10^{-4}, 1 \times 10^{-4}, 5 \times 10^{-5}, 1 \times 10^{-5}]$.

For characterization and diagnosis tasks, features extracted by the model’s backbone were passed through a Multi-Layer Perceptron (MLP) classification head to map them to the class dimension. These models were trained using a cross-entropy loss function. For prognosis tasks, the same backbone architecture was used, but the extracted features were mapped to a single risk score via an MLP. Prognostic models were trained using the Cox Proportional Hazards (CoxPH) model, leveraging a partial log-likelihood loss function to account for censored data. While our dataset included three prognostic labels (recurrence-free survival (RFS), defined as the interval from surgery to local recurrence, distant metastasis, or renal cancer-related death; disease-specific survival (DSS), the interval from surgery to death from renal cancer; and overall survival (OS), the interval from surgery to death from any cause), we exclusively utilized the RFS label for model training. The trained RFS model was then used to calculate risk scores across all three survival endpoints (RFS, DSS, and OS) for quantitative evaluation.

4.4.4 Radiology report generation

We developed a caption generation model, adapted from the LLaVA framework^{66,67}, designed to interpret 3D renal CT volumes. This model integrates the frozen RenalCLIP image backbone $f_{\text{backbone}}(\cdot)$, a multi-modal projector, and an LLM. The image backbone processes 3D renal CT volumes, compressing them into a feature space. These features are then passed to our multi-modal projector, which is implemented as a simple linear layer. This layer linearly transforms the image features, converting them from their original dimension (e.g., 512) into a dimension compatible with the LLM’s hidden size (e.g., 4,096). This effectively functions as a visual tokenizer, aligning the image features with the LLM’s word embedding space. For the LLM component, we employed BioMistral-7B⁶⁸, a version of Mistral-7B further pre-trained on medical textual data from PubMed Central Open Access, making it well-suited for the medical domain; its architecture includes 32 transformer layers, 32 attention heads, an embedding dimension of 4,096, a hidden dimension of 14,336, and a vocabulary size of 32,000.

The captioning model undergoes a two-step training strategy. In both steps, the model is guided by a consistent instruction prompt structured as follows:

```
<s>[INST]
    Generate a radiology report for the given CT scan of suspected
    renal cancer.
```

```
Use the following format:  
Findings: [Detailed observations based on the CT scan.]  
Impression: [Summary of the diagnostic conclusions.]  
[/INST]
```

First, in the initial alignment step, only the multi-modal projector is trained while both the image backbone and the LLM remain frozen, utilizing the train set of our internal pre-training dataset. This step is crucial for aligning the multi-modal projector in biomedical concept space and enhancing subsequent fine-tuning performance. Second, in the fine-tuning step, training continues for the multi-modal projector (image backbone remains frozen), but the LLM is fine-tuned using LoRA⁵⁹, utilizing the internal training cohort. All training for the captioning model, across both steps, was conducted on a single A100-80GB GPU with a batch size of 30. In the initial alignment step, the projector was trained for 20 epochs using a learning rate of 1×10^{-3} . After each epoch, performance was validated on the validation set of the pre-training dataset, and the checkpoint with the lowest validation loss was saved. For the subsequent fine-tuning step, the projection layer’s learning rate was set to 5×10^{-4} , while the LoRA weights for the LLM were fine-tuned with a learning rate of 1×10^{-6} over 2 epochs. More hyperparameters for both pre-training and fine-tuning in radiology report generation are detailed in Supplementary Tables 41–42.

4.4.5 Zero-shot classification

For zero-shot classification, we employed a method that adapts CLIP’s original framework³³. For each class, we generated a text prompt by combining a class prompt (e.g., ‘benign’ for malignancy assessment) with a pre-defined sentence template. For example, a template might be ‘A soft tissue mass that is {...} is visible in the kidney.’ In total, 20 distinct templates were used and each class was associated with five different class prompts, resulting in 100 unique text prompts generated for every class. A comprehensive list of all class names and templates used is provided in Supplementary Tables 24–26.

To rigorously evaluate model performance while accounting for the variability arising from this diverse prompt set, we implemented and compared two distinct zero-shot evaluation strategies.

First, to determine a robust, high-performance metric, we employed a maximum similarity ensemble strategy. For each image embedding u_i , we computed its cosine similarity against the entire set of 100 pre-computed text embeddings for each class $c \in \{0, 1\}$, denoted as $\{\mathbf{v}_{c,k}\}_{k=1}^{100}$, where k indexes the unique prompts for a given class. The maximum similarity score within each class set was then taken as the definitive logit for that class, i.e., $s_c = \max_k(\text{sim}(\mathbf{u}_i, \mathbf{v}_{c,k}))$. An image was assigned to the class with the highest logit score.

Second, to specifically quantify the model’s sensitivity to prompt selection, we employed a stochastic prompt sampling strategy. In this analysis, we performed B bootstrap iterations (e.g., $B = 1000$). For each iteration, we randomly sampled a single prompt embedding for the positive class and one for the negative class to form a classifier pair. This pair was then used to evaluate the model’s ROC AUC across the entire test cohort. This procedure yielded a distribution of performance scores,

from which we report the mean and 95% confidence interval to visualize the model’s sensitivity.

4.4.6 Cross-modal retrieval

For zero-shot retrieval, we employed a method analogous to our zero-shot classification approach, operating within the same aligned latent space. For text-to-image retrieval, a specific text query (e.g., a radiology report) was used to find the top-K closest CT volumes. Conversely, image-to-text retrieval was performed by querying with a CT volume to find the nearest text entries.

4.4.7 Ablation studies

Impact of uni-modal pre-training components

We next sought to dissect the contributions of the uni-modal pre-training stages that precede the final cross-modality alignment in RenalCLIP. We conducted an ablation study comparing the full RenalCLIP model against three ablated versions: (1) a model pairing our pre-trained image encoder with the general BioClinicalBERT⁶⁹ model, thus omitting our domain-specific text pre-training (termed ‘RenalCLIP w/o Text Pre-train’); (2) a model pairing our domain-specific pre-trained text encoder with a randomly initialized 3D ResNet-18 image encoder (termed ‘RenalCLIP w/o Image Pre-train’); and (3) a baseline model combining the randomly initialized image encoder and the general BioClinicalBERT text encoder (termed ‘CLIP Baseline’). The comprehensive comparison across cross-modality retrieval, zero-shot classification, and fine-tuning tasks is presented in Extended Data Fig. 8.

We found that for cross-modality retrieval, a clear performance hierarchy emerged, with the full RenalCLIP model performing best, followed by the model with only text pre-training, then the model with only image pre-training, and finally the baseline. A similar trend was noted in fine-tuning for renal scoring and diagnosis, where the full RenalCLIP and the model with only image pre-training performed comparably and were superior to the other two models, with text pre-training still providing a benefit over the baseline.

The zero-shot classification results presented a more nuanced picture that was dependent on the evaluation strategy. Using the deterministic maximum similarity ensemble strategy, the full RenalCLIP again achieved the highest performance, followed by the model with only image pre-training. Conversely, when evaluated using the stochastic prompt sampling strategy to assess prompt sensitivity, the model with only image pre-training slightly outperformed the full RenalCLIP model. This finding suggests that while our domain-specific text pre-training is highly effective for the deterministic ensemble approach, it may also introduce an increased sensitivity to prompt phrasing variations, a phenomenon that warrants further investigation.

Overall, these findings establish that domain-specific image pre-training provides the most substantial and consistent performance foundation across all tasks. Our renal-specific text pre-training offers a crucial synergistic benefit, particularly for fine-grained retrieval and robust zero-shot classification.

Impact of multi-phase CT inputs

To investigate the marginal benefit of integrating multi-phase data, we conducted an ablation study evaluating four cumulative input settings: single-phase (A), dual-phase (A and V, termed ‘AV’), tri-phase (N, A, and V, termed ‘NAV’), and the full quad-phase (N, A, V, and D, termed ‘NAVD’) (Extended Data Fig. 9c–e).

Our results reveal a nuanced trade-off. While multi-phase fusion strategies generally yielded a modest performance gain over the single-phase input across RENAL scoring, diagnosis, and survival prognosis, this single-phase model itself established a remarkably strong baseline. Consequently, we observed no universally optimal phase combination; the best-performing configuration varied depending on the specific downstream task and patient cohort. For instance, while the quad-phase input occasionally yielded the highest performance, the dual-phase (AV) or tri-phase (NAV) inputs proved superior in other settings.

We hypothesize that this complex relationship stems from a trade-off between accumulating diagnostic signal and introducing potential noise, a dynamic amplified by our simple logit-averaging fusion method. Although additional phases offer supplementary information (e.g., washout patterns), they can also introduce confounding features that dilute the primary signal, particularly when imaging characteristics vary across cohorts. These findings suggest that while multi-phase data holds clear value, the optimal strategy is not a simple aggregation of all available information. Instead, future work on more sophisticated, learnable fusion mechanisms is warranted, and for current applications, the selection of CT phases should be tailored to the specific clinical question.

4.4.8 Statistical analysis

To assess statistical uncertainty, 95% confidence intervals (CIs) for all reported performance metrics were estimated using a non-parametric bootstrap method with 1,000 resamples. A two-sided p-value of less than 0.05 was considered statistically significant for all hypothesis tests. The analyses focused on three prognostic endpoints: RFS, DSS, and OS. For all survival analyses, the cohort was restricted to patients with malignant tumors. For risk stratification, each model’s continuous risk score was first dichotomized into high- and low-risk groups based on the cohort-specific median. Kaplan-Meier curves were plotted to visualize survival differences, which were assessed for significance using the log-rank test. These univariate survival analyses were performed using the lifelines library (version 0.30.0) in Python. To determine the independent prognostic value of each derived risk score, a multivariate Cox proportional hazards regression model was constructed using SPSS Statistics 21.0. The significance of each variable in the model was assessed using the Wald test. In this multivariate analysis, each model’s risk score was included as a continuous variable, and the model was adjusted for established clinical and pathological risk factors such as TNM stage and WHO/ISUP grade.

Computing hardware and software. Scripts for 3D CT pre-processing were written in Python (version 3.10.14) using the libraries Nibabel (version 5.3.1), Numpy (version 1.26.4), and Scipy (version 1.13.1). The multi-stage pre-training of RenalCLIP

was conducted on NVIDIA A100 80GB GPUs using PyTorch (version 2.3.0) with CUDA 12.1. The initial image encoder pre-training utilized a single GPU, with data augmentation implemented via MONAI (version 1.3.1). The subsequent text encoder pre-training was also performed on a single GPU, leveraging the LLM2Vec (version 0.2.2), Transformers (version 4.44.2), flash-attn (version 2.7.2), and PEFT (version 0.10.0) libraries. The final cross-modal pre-training was performed on four GPUs configured for multi-GPU, single-node training using PyTorch’s DistributedDataParallel (DDP) framework. All downstream task fine-tuning experiments were conducted on a single 80GB NVIDIA A100 GPU. The software environment was consistent with pre-training (Python 3.10.14, PyTorch 2.3.0, CUDA 12.1, MONAI 1.3.1). Specific tasks required additional libraries: PyCox (version 0.3.0) was used for prognosis tasks, while PEFT (version 0.10.0) and Transformers (version 4.40.2) were used for report generation. Performance metrics were calculated using several Python libraries. Standard classification metrics, including AUROC, PRAUC, sensitivity, specificity, and the F1-score, were computed using Scikit-learn (version 1.5.0). C-index was calculated using PyCox (version 0.3.0), while the time-dependent versions of the ROC AUC, C-index, and Brier score were calculated using scikit-survival (version 0.24.1). Natural language generation metrics were evaluated using NLTK (version 3.9.1) for BLEU and METEOR, and rouge-score (version 0.1.2) for ROUGE. Implementation of the comparative baseline models was based on the official configurations provided in their respective repositories: CT-CLIP (<https://github.com/ibrahimethemhamamci/CT-CLIP>), Merlin (<https://github.com/StanfordMIMI/Merlin>), CT-FM (<https://github.com/project-lighter/CT-FM>), RadFM (<https://github.com/chaoyi-wu/RadFM>), CT-CHAT (<https://github.com/ibrahimethemhamamci/CT-CHAT>), GPT-4o (<https://ai.azure.com/catalog/models/gpt-4o>), and MedGemma (<https://huggingface.co/google/medgemma-4b-it>).

Code availability. The source code for all experiments, pre-trained model weights for RenalCLIP, and tutorial Jupyter notebooks for key applications are publicly available on GitHub to support reproducibility and further research (<https://github.com/dt-yuhui/RenalCLIP>). All experiments are documented in detail in the Methods section to ensure transparency and facilitate the independent replication of our findings.

Acknowledgements. This study was funded by grants from the National Key Research and Development Program of China [2024YFF1207500(S. Wang)], National Natural Science Foundation of China [81902563 (Y. Xiong), 81974393 (J. Guo)], Hexi University President Fund Innovation Team Project [CXTD2022012 (J. Yao)], International Science and Technology Cooperation Program under the 2023 Shanghai Action Plan for Science [(23410710400) (S. Wang)] and Shanghai Municipal Education Commission Project for Promoting Research Paradigm Reform and Empowering Disciplinary Advancement through Artificial Intelligence [SOF101020 (S. Wang)]. All these study sponsors have no roles in the study design, in the collection, analysis and interpretation of data. We thank pathologists Qi Sun (Fudan University) and Haiyue Lin (the First People’s Hospital of Lianyungang) for re-evaluating pathologic

slides. We thank radiologists Xiaoxia Li (Fudan University) and Linpeng Yao (Zhejiang University) for assessing R.E.N.A.L. score. The computations in this research were performed using the CFFF platform of Fudan University.

Author contributions. Y. Tao, Z. Zhao, Z. Wang, X. Luo, and F. Chen contributed to data acquisition, analysis, interpretation, statistical analysis, and manuscript drafting. K. Wang, C. Wu, X. Zhang, S. Zhang, J. Yao, X. Jin, X. Jiang, Y. Yang, D. Li, and L. Qiu provided technical and material support and participated in statistical analyses. Y. Tao, K. Wang, Z. Wang, X. Luo, and S. Wang were responsible for algorithm development and statistical analyses. Z. Shao, J. Guo, N. Yu, S. Wang and Y. Xiong designed the study, interpreted data, drafted and revised the manuscript, secured funding, and supervised the study. All authors critically reviewed the manuscript, approved the final version, and agree to be accountable for all aspects of the work.

Competing interests. The authors declare no competing interests.

References

- [1] Wong, M. C. *et al.* Incidence and mortality of kidney cancer: temporal patterns and global trends in 39 countries. *Scientific reports* **7**, 15698 (2017).
- [2] Turner, R. M. n., Morgan, T. M. & Jacobs, B. L. Epidemiology of the small renal mass and the treatment disconnect phenomenon. *Urologic Clinics of North America* **44**, 147–154 (2017). Epub 2017 Mar 14.
- [3] Gill, I. S. *et al.* Comparison of 1,800 laparoscopic and open partial nephrectomies for single renal tumors. *The Journal of urology* **178**, 41–46 (2007).
- [4] Bhindi, B. *et al.* The probability of aggressive versus indolent histology based on renal tumor size: implications for surveillance and treatment. *European urology* **74**, 489–497 (2018).
- [5] Wentland, A. L. *et al.* Differentiation of benign from malignant solid renal lesions using ct-based radiomics and machine learning: comparison with radiologist interpretation. *Abdominal Radiology* **48**, 642–648 (2023).
- [6] Silverman, S. G., Gan, Y. U., Morteale, K. J., Tuncali, K. & Cibas, E. S. Renal masses in the adult patient: the role of percutaneous biopsy. *Radiology* **240**, 6–22 (2006).
- [7] Tomaszewski, J. J., Uzzo, R. G. & Smaldone, M. C. Heterogeneity and renal mass biopsy: a review of its role and reliability. *Cancer biology & medicine* **11**, 162–172 (2014).
- [8] Patel, H. D. *et al.* Diagnostic accuracy and risks of biopsy in the diagnosis of a renal mass suspicious for localized renal cell carcinoma: systematic review of the literature. *The Journal of urology* **195**, 1340–1347 (2016).
- [9] Bjurlin, M. A. *et al.* Influence of renal biopsy results on the management of small kidney cancers in older patients: Results from a population-based cohort. *Urologic Oncology: Seminars and Original Investigations*, Vol. 35, 604–e1 (Elsevier, 2017).
- [10] Leibovich, B. C. *et al.* Predicting oncologic outcomes in renal cell carcinoma after surgery. *European urology* **73**, 772–780 (2018).
- [11] Klatte, T., Rossi, S. H. & Stewart, G. D. Prognostic factors and prognostic models for renal cell carcinoma: a literature review. *World journal of urology* **36**, 1943–1952 (2018).
- [12] Rosellini, M. *et al.* Prognostic and predictive biomarkers for immunotherapy in advanced renal cell carcinoma. *Nature Reviews Urology* **20**, 133–157 (2023).
- [13] Choueiri, T. K. *et al.* Adjuvant pembrolizumab after nephrectomy in renal-cell carcinoma. *New England Journal of Medicine* **385**, 683–694 (2021).

- [14] Braun, D. A. *et al.* Clinical validation of pbrm1 alterations as a marker of immune checkpoint inhibitor response in renal cell carcinoma. *JAMA oncology* **5**, 1631–1633 (2019).
- [15] Ged, Y. *et al.* Dna damage repair pathway alterations in metastatic clear cell renal cell carcinoma and implications on systemic therapy. *Journal for immunotherapy of cancer* **8**, e000230 (2020).
- [16] Xiong, Y. *et al.* Identification and validation of dichotomous immune subtypes based on intratumoral immune cells infiltration in clear cell renal cell carcinoma patients. *Journal for immunotherapy of cancer* **8**, e000447 (2020).
- [17] Paschali, M. *et al.* Foundation models in radiology: What, how, why, and why not. *Radiology* **314**, e240597 (2025).
- [18] Aggarwal, R. *et al.* Diagnostic accuracy of deep learning in medical imaging: a systematic review and meta-analysis. *NPJ digital medicine* **4**, 65 (2021).
- [19] Zhang, K. *et al.* A generalist vision–language foundation model for diverse biomedical tasks. *Nature Medicine* 1–13 (2024).
- [20] Wang, Z., Wu, Z., Agarwal, D. & Sun, J. *Medclip: Contrastive learning from unpaired medical images and text. Proceedings of the Conference on Empirical Methods in Natural Language Processing. Conference on Empirical Methods in Natural Language Processing*, Vol. 2022, 3876 (2022).
- [21] You, K. *et al.* *Cxr-clip: Toward large scale chest x-ray language-image pre-training. International Conference on Medical Image Computing and Computer-Assisted Intervention*, 101–111 (Springer, 2023).
- [22] Lu, M. Y. *et al.* A visual-language foundation model for computational pathology. *Nature medicine* **30**, 863–874 (2024).
- [23] Lu, Z., Li, H., Parikh, N. A., Dillman, J. R. & He, L. Radclip: Enhancing radiologic image analysis through contrastive language–image pretraining. *IEEE Transactions on Neural Networks and Learning Systems* (2025).
- [24] Shi, D. *et al.* A multimodal visual–language foundation model for computational ophthalmology. *npj Digital Medicine* **8**, 381 (2025).
- [25] Zhou, Y. *et al.* A foundation model for generalizable disease detection from retinal images. *Nature* **622**, 156–163 (2023).
- [26] Qiu, J. *et al.* Visionfm: a multi-modal multi-task vision foundation model for generalist ophthalmic artificial intelligence. *arXiv preprint arXiv:2310.04992* (2023).

- [27] Xu, H. *et al.* A whole-slide foundation model for digital pathology from real-world data. *Nature* **630**, 181–188 (2024).
- [28] Chen, R. J. *et al.* Towards a general-purpose foundation model for computational pathology. *Nature Medicine* **30**, 850–862 (2024).
- [29] Clark, K. *et al.* The cancer imaging archive (tcia): maintaining and operating a public information repository. *Journal of digital imaging* **26**, 1045–1057 (2013).
- [30] Dubey, A. *et al.* The llama 3 herd of models. *arXiv e-prints* arXiv:2407 (2024).
- [31] BehnamGhader, P. *et al.* Llm2vec: Large language models are secretly powerful text encoders. *arXiv preprint arXiv:2404.05961* (2024).
- [32] Huang, W. *et al.* Llm2clip: Powerful language model unlocks richer visual representation. *arXiv preprint arXiv:2411.04997* (2024).
- [33] Radford, A. *et al.* Learning transferable visual models from natural language supervision. *International conference on machine learning*, 8748–8763 (PmLR, 2021).
- [34] He, K., Zhang, X., Ren, S. & Sun, J. *Deep residual learning for image recognition. Proceedings of the IEEE conference on computer vision and pattern recognition*, 770–778 (2016).
- [35] Hamamci, I. E. *et al.* A foundation model utilizing chest ct volumes and radiology reports for supervised-level zero-shot detection of abnormalities. *CoRR* (2024).
- [36] Blankemeier, L. *et al.* Merlin: A vision language foundation model for 3d computed tomography. *Research Square* rs-3 (2024).
- [37] Pai, S. *et al.* Vision foundation models for computed tomography. *arXiv preprint arXiv:2501.09001* (2025).
- [38] Kutikov, A. & Uzzo, R. G. The renal nephrometry score: a comprehensive standardized system for quantitating renal tumor size, location and depth. *The Journal of urology* **182**, 844–853 (2009).
- [39] Tanno, R. *et al.* Collaboration between clinicians and vision–language models in radiology report generation. *Nature Medicine* **31**, 599–608 (2025).
- [40] Hurst, A. *et al.* Gpt-4o system card. *arXiv preprint arXiv:2410.21276* (2024).
- [41] Sellergren, A. *et al.* Medgemma technical report. *arXiv preprint arXiv:2507.05201* (2025).
- [42] Wu, C., Zhang, X., Zhang, Y., Wang, Y. & Xie, W. Towards generalist foundation model for radiology by leveraging web-scale 2d&3d medical data. *arXiv preprint*

- arXiv:2308.02463* (2023).
- [43] Schieda, N. *et al.* Active surveillance of renal masses: the role of radiology. *Radiology* **302**, 11–24 (2022).
 - [44] Li, Y. *et al.* Histopathologic and proteogenomic heterogeneity reveals features of clear cell renal cell carcinoma aggressiveness. *Cancer cell* **41**, 139–163 (2023).
 - [45] Zheng, Z., Chen, Z., Xie, Y., Zhong, Q. & Xie, W. Development and validation of a ct-based nomogram for preoperative prediction of clear cell renal cell carcinoma grades. *European radiology* **31**, 6078–6086 (2021).
 - [46] Nie, P. *et al.* A ct-based deep learning radiomics nomogram outperforms the existing prognostic models for outcome prediction in clear cell renal cell carcinoma: a multicenter study. *European Radiology* **33**, 8858–8868 (2023).
 - [47] Topol, E. J. High-performance medicine: the convergence of human and artificial intelligence. *Nature medicine* **25**, 44–56 (2019).
 - [48] Rajpurkar, P., Chen, E., Banerjee, O. & Topol, E. J. Ai in health and medicine. *Nature medicine* **28**, 31–38 (2022).
 - [49] Yap, F. Y. *et al.* Shape and texture-based radiomics signature on ct effectively discriminates benign from malignant renal masses. *European radiology* **31**, 1011–1021 (2021).
 - [50] Demirjian, N. L. *et al.* Ct-based radiomics stratification of tumor grade and tnm stage of clear cell renal cell carcinoma. *European Radiology* **32**, 2552–2563 (2022).
 - [51] Xiong, Y. *et al.* Artificial intelligence links ct images to pathologic features and survival outcomes of renal masses. *Nature Communications* **16**, 1425 (2025).
 - [52] Isensee, F., Jaeger, P. F., Kohl, S. A., Petersen, J. & Maier-Hein, K. H. nnu-net: a self-configuring method for deep learning-based biomedical image segmentation. *Nature methods* **18**, 203–211 (2021).
 - [53] Dai, C. *et al.* Deep learning assessment of small renal masses at contrast-enhanced multiphase ct. *Radiology* **311**, e232178 (2024).
 - [54] Rosenfeld, E., Nakkiran, P., Pouransari, H., Tuzel, O. & Faghri, F. Ape: Aligning pretrained encoders to quickly learn aligned multimodal representations. *arXiv preprint arXiv:2210.03927* (2022).
 - [55] Yang, J., Wu, Z., Zhao, Y. & Ma, Y. Language-image alignment with fixed text encoders. *arXiv preprint arXiv:2506.04209* (2025).
 - [56] Boecking, B. *et al.* Making the most of text semantics to improve biomedical vision–language processing. *European conference on computer vision*, 1–21

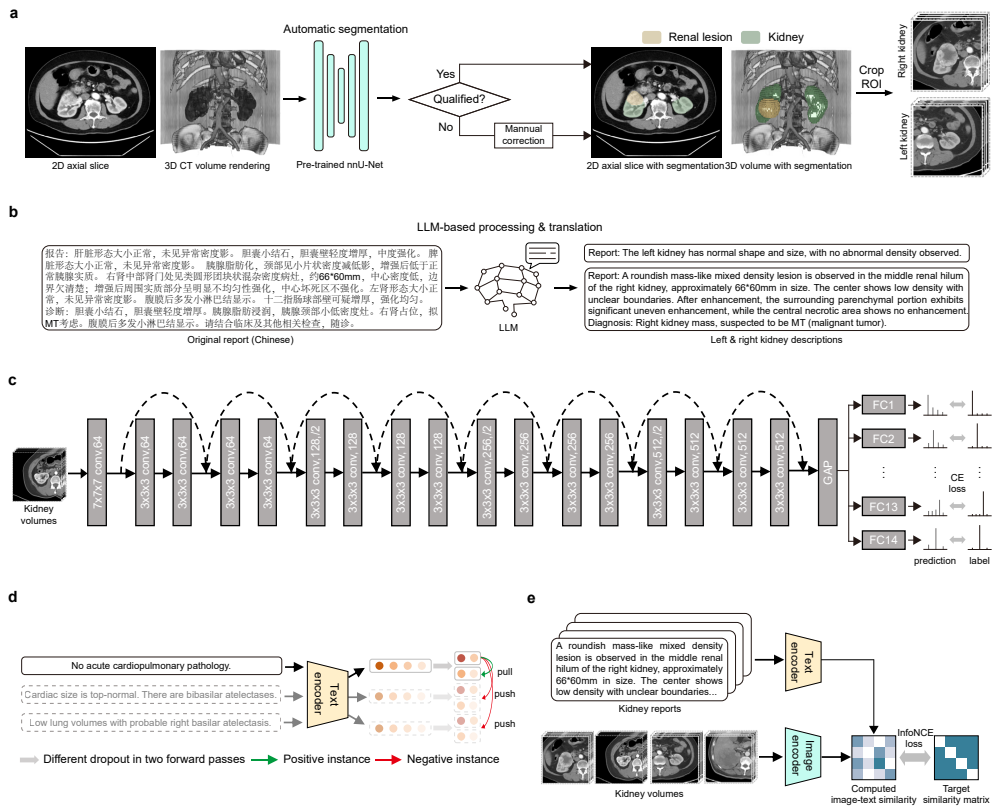
(Springer, 2022).

- [57] Devlin, J., Chang, M.-W., Lee, K. & Toutanova, K. *Bert: Pre-training of deep bidirectional transformers for language understanding. Proceedings of the 2019 conference of the North American chapter of the association for computational linguistics: human language technologies, volume 1 (long and short papers)*, 4171–4186 (2019).
- [58] Liu, Y. *et al.* Roberta: A robustly optimized bert pretraining approach. *arXiv preprint arXiv:1907.11692* (2019).
- [59] Hu, E. J. *et al.* Lora: Low-rank adaptation of large language models. *ICLR* **1**, 3 (2022).
- [60] Johnson, A. E. *et al.* Mimic-cxr, a de-identified publicly available database of chest radiographs with free-text reports. *Scientific data* **6**, 317 (2019).
- [61] Gao, T., Yao, X. & Chen, D. Simcse: Simple contrastive learning of sentence embeddings. *arXiv preprint arXiv:2104.08821* (2021).
- [62] Loshchilov, I. & Hutter, F. Decoupled weight decay regularization. *arXiv preprint arXiv:1711.05101* (2017).
- [63] Chen, T., Xu, B., Zhang, C. & Guestrin, C. Training deep nets with sublinear memory cost. *arXiv preprint arXiv:1604.06174* (2016).
- [64] Myronenko, A. *3d mri brain tumor segmentation using autoencoder regularization. International MICCAI brainlesion workshop*, 311–320 (Springer, 2018).
- [65] Dosovitskiy, A. *et al.* An image is worth 16x16 words: Transformers for image recognition at scale. *arXiv preprint arXiv:2010.11929* (2020).
- [66] Liu, H., Li, C., Wu, Q. & Lee, Y. J. Visual instruction tuning. *Advances in neural information processing systems* **36**, 34892–34916 (2023).
- [67] Li, C. *et al.* Llava-med: Training a large language-and-vision assistant for biomedicine in one day. *Advances in Neural Information Processing Systems* **36**, 28541–28564 (2023).
- [68] Labrak, Y. *et al.* Biomistral: A collection of open-source pretrained large language models for medical domains. *arXiv preprint arXiv:2402.10373* (2024).
- [69] Alsentzer, E. *et al.* Publicly available clinical bert embeddings. *arXiv preprint arXiv:1904.03323* (2019).

Feature	Pre-training cohort	Internal training cohort	Internal validation cohort	Xiamen cohort	Shandong cohort	Ruijing cohort	Lianyun cohort	Zhangye cohort	TCIA cohort
	N=6867	N=400	N=100	N=251	N=250	N=229	N=220	N=67	N=425
Number of CT volumes	21819	1240	316	796	991	727	671	259	1047
CT phases (%)									
Non-contrast phase	5756(83.8)	339(84.8)	78(78.0)	199(79.3)	250(100.0)	214(93.4)	186(84.5)	66(98.5)	293(68.9)
Arterial phase	6799(99.0)	400(100.0)	100(100.0)	249(99.2)	249(99.6)	208(90.8)	220(100.0)	67(100.0)	238(56.0)
Venous phase	6642(96.7)	391(97.8)	98(98.0)	246(98.0)	248(99.2)	215(93.9)	211(95.9)	65(97.0)	293(68.9)
Delayed phase	2622(38.2)	110(27.5)	40(40.0)	102(40.6)	244(97.6)	90(39.3)	54(24.5)	61(91.0)	223(52.5)
Median age (IQR)	56(48,65)	57(50,65)	57(48,65)	53(43,63)	57(51,65)	59(50,67)	57(51,65)	58(48,66)	59(51,68)
Male sex (%)	4232(61.6)	259(64.8)	62(62.0)	144(57.4)	149(59.6)	142(62.0)	123(55.9)	36(53.7)	261(62.1)
Median tumor size (IQR)	3.6(2.5,5.5)	3.5(2.5,5.5)	3.8(2.6,5.4)	3.8(2.5,5.0)	3.8(2.4,5.0)	5.0(3.5,7.0)	4.0(3.0,5.7)	5.8(3.7,7.0)	4.5(3.0,6.9)
TNM stage (%)									
I	4467(65.1)	288(72.0)	64(64.0)	149(59.4)	179(71.6)	118(51.5)	145(65.9)	31(46.3)	244(57.4)
II	460(6.7)	20(5.0)	9(9.0)	13(5.2)	13(5.2)	33(14.4)	20(9.1)	15(22.4)	33(7.8)
III	594(8.7)	26(6.5)	12(12.0)	13(5.2)	28(11.2)	25(10.9)	7(3.2)	7(10.4)	89(20.9)
IV	86(1.3)	1(0.3)	1(1.0)	3(1.2)	2(0.8)	14(6.1)	1(0.5)	1(1.5)	45(10.6)
Not applicable	1260(18.3)	65(16.3)	14(14.0)	73(29.1)	28(11.2)	39(17.0)	47(21.4)	13(19.4)	14(3.3)
WHO/ISUP Grade^a (%)									
Low (1 & 2)	3745(54.5)	232(58.1)	51(51.0)	128(51.0)	149(59.6)	88(38.4)	115(52.2)	20(29.9)	184(43.3)
High (3 & 4)	1020(14.8)	56(14.1)	22(22.0)	17(6.8)	59(23.6)	63(27.5)	17(7.8)	28(41.8)	191(44.9)
Absence or not applicable	2102(30.7)	112(28.0)	27(27.0)	106(42.2)	42(16.8)	78(34.1)	88(40.0)	19(28.4)	50(11.8)
Necrosis^c (%)	610(8.9)	41(10.3)	12(12.0)	14(5.6)	30(12.0)	28(12.2)	12(5.5)	17(25.4)	72(16.9)
Sarcomatoid differentiation^d (%)	115(1.7)	7(1.8)	7(7.0)	6(2.4)	2(0.8)	3(1.3)	2(0.9)	2(3.0)	16(3.8)
Histologic classification (%)									
Benign and indolent (%)	1260(18.3)	65(16.3)	14(14.0)	73(29.1)	28(11.2)	39(17.0)	47(21.4)	13(19.4)	14(3.3)
Angiomyolipoma	674(9.8)	43(10.8)	8(8.0)	53(21.1)	17(6.8)	28(12.2)	17(7.7)	6(9.0)	3(0.7)
Complex renal cyst	436(6.3)	11(2.8)	2(2.0)	17(6.8)	7(2.8)	6(2.6)	23(10.5)	5(7.5)	0
Oncocytoma	67(1.0)	5(1.3)	3(3.0)	2(0.8)	4(1.6)	4(1.7)	6(2.7)	0	9(2.1)
Mixed epithelial and stromal renal tumors	20(0.3)	0	0	0	0	0	1(0.5)	0	2(0.5)
Metanephric tumors	10(0.1)	2(0.5)	0	1(0.4)	0	0	0	0	0
Other benign masses ^b	53(0.8)	4(1.0)	1(1.0)	0	0	1(1.6)	0	2(3.0)	0
Malignant and indolent (%)	3837(55.9)	256(64.0)	54(54.0)	148(59.0)	142(56.8)	97(42.4)	130(59.1)	22(32.8)	204(48.0)
Indolent clear cell RCC ^e	3158(46.0)	206(51.5)	42(42.0)	117(46.6)	119(47.6)	79(34.6)	97(44.1)	15(22.4)	148(34.8)
Indolent papillary RCC ^f	195(2.8)	12(3.0)	3(3.0)	4(1.6)	13(5.2)	2(0.9)	10(4.5)	1(1.5)	24(5.6)
Chromophobe RCC	280(4.1)	25(6.3)	9(9.0)	19(7.6)	10(4.0)	9(3.9)	12(5.5)	6(9.0)	30(7.1)
Clear cell papillary renal cell tumor	30(0.4)	3(0.8)	0	3(1.2)	0	0	3(1.4)	0	0
Multifocal cystic renal neoplasm of low malignant potential	57(0.8)	3(0.8)	0	1(0.4)	0	7(3.1)	3(1.4)	0	1(0.2)
Epithelioid angiomyolipoma	46(0.7)	6(1.5)	0	3(1.2)	0	0	1(0.5)	0	0
Other indolent tumors ^g	71(1.0)	1(0.3)	0	1(0.4)	0	0	4(1.8)	0	1(0.2)
Malignant and aggressive (%)	1680(24.5)	77(19.3)	31(31.0)	30(12.0)	80(32.0)	92(40.2)	31(14.1)	32(47.8)	207(48.7)
Aggressive clear cell RCC	1373(20.0)	62(15.5)	27(27.0)	20(8.0)	68(27.2)	75(32.8)	22(10)	28(41.8)	192(45.2)
Aggressive papillary RCC	103(1.5)	8(2.0)	1(1.0)	4(1.6)	8(3.2)	7(3.1)	3(1.4)	4(6.0)	11(2.6)
TEF-3 rearranged RCC ^h	52(0.8)	1(0.3)	1(1.0)	5(2.0)	3(1.2)	1(0.4)	4(1.8)	0	0
Renal cell carcinoma, NOS	49(0.7)	3(0.8)	1(1.0)	1(0.4)	1(0.4)	4(1.7)	1(0.5)	0	2(0.5)
Sarcomas ⁱ	17(0.2)	3(0.8)	1(1.0)	0	0	1(0.4)	0	0	0
Other aggressive tumors ^j	86(1.3)	0	0	0	0	4(1.7)	1(0.5)	0	2(0.5)
Malignant and indeterminate^k (%)	90(1.3)	2(0.5)	1(1.0)	0	0	1(0.4)	12(5.5)	0	0

a. WHO/ISUP grade was evaluated in clear cell RCC and papillary RCC only. Necrosis and sarcomatoid differentiation were evaluated in malignant tumors. Any sarcomatoid differentiation led to the classification of malignancies. b. Other benign masses included hemangioma, leiomyoma, schwannoma, etc. c. Clear cell RCC and papillary RCC with high-grade (3-4) components, sarcomatoid differentiation or evasion into major veins or perinephric tissues were classified as aggressive. The presence of coagulative necrosis also led to the classification as aggressive for clear cell RCC but not for papillary RCC. d. Other indolent tumors included mucinous tubular and spindle cell carcinoma, tubulocystic RCC, eosinophilic solid and cystic RCC, etc. e. Xp11 translocation RCC and melanotic Xp11 translocation RCC followed an aggressive course. f. Sarcomas included rhabdomyosarcoma, synovial sarcoma, Ewing sarcoma, etc. g. Other aggressive tumors included collecting carcinoma, renal medullary carcinoma, indolent subtypes with sarcomatoid differentiation, etc. h. The aggressiveness for some of the tumors with missing information of tumor grade, immunohistochemistry or genetic testing were unclear.

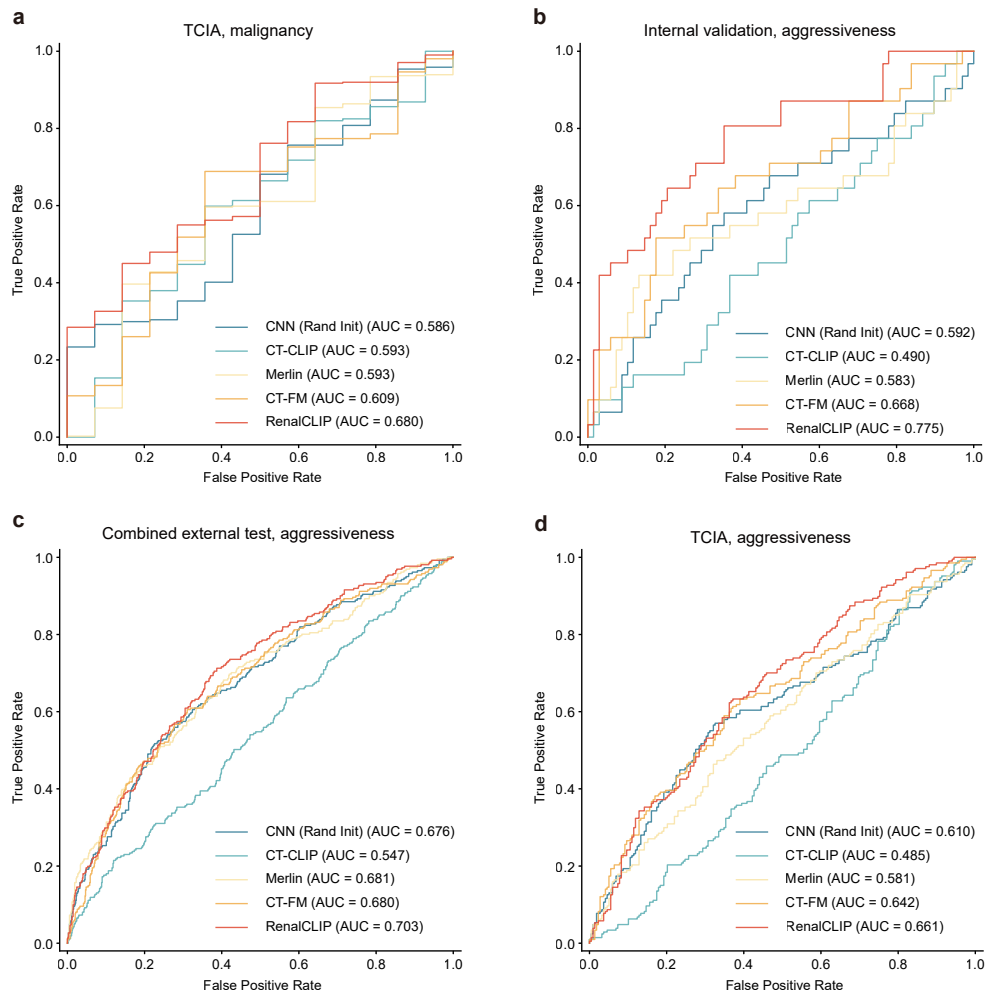
Extended Data Table 1 | Baseline clinicopathologic and imaging characteristics of the study cohorts.



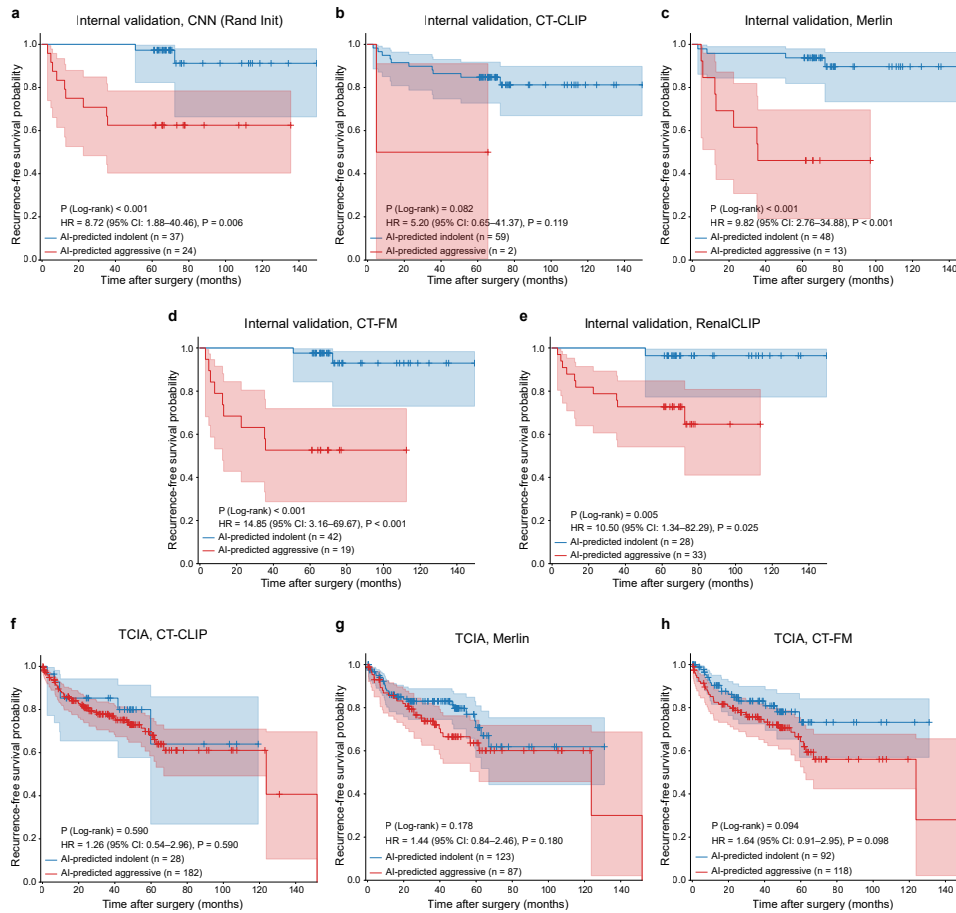
Extended Data Fig. 1 | Data processing and RenalCLIP pre-training architecture. **a**, Semi-automated ROI localization pipeline: initial nnU-Net segmentations of the kidney and lesion undergo expert review and are manually corrected if necessary, before a bounding box is computed from the final mask to crop the single-kidney ROI. **b**, Processing of original Chinese radiology reports, involving LLM-based partitioning into ‘left kidney’ and ‘right kidney’ descriptions, followed by programmatic translation into English. **c**, Architecture of the knowledge-enhanced image encoder, featuring a 3D ResNet-18 backbone pre-trained via a multi-task learning framework to predict 14 structured attributes, each with a corresponding fully connected (FC) layer as its prediction head, optimized by cross-entropy (CE) loss. **d**, The SimCSE methodology for text encoder refinement, which maximizes the similarity between two distinct representations of a single input sentence (generated via different dropout masks, positive instance) while minimizing their similarity to other sentences in the batch (negative instance). **e**, The overall vision-language framework, where the knowledge-enhanced image and text encoders project images and their corresponding text into a joint embedding space for alignment via the InfoNCE loss objective.



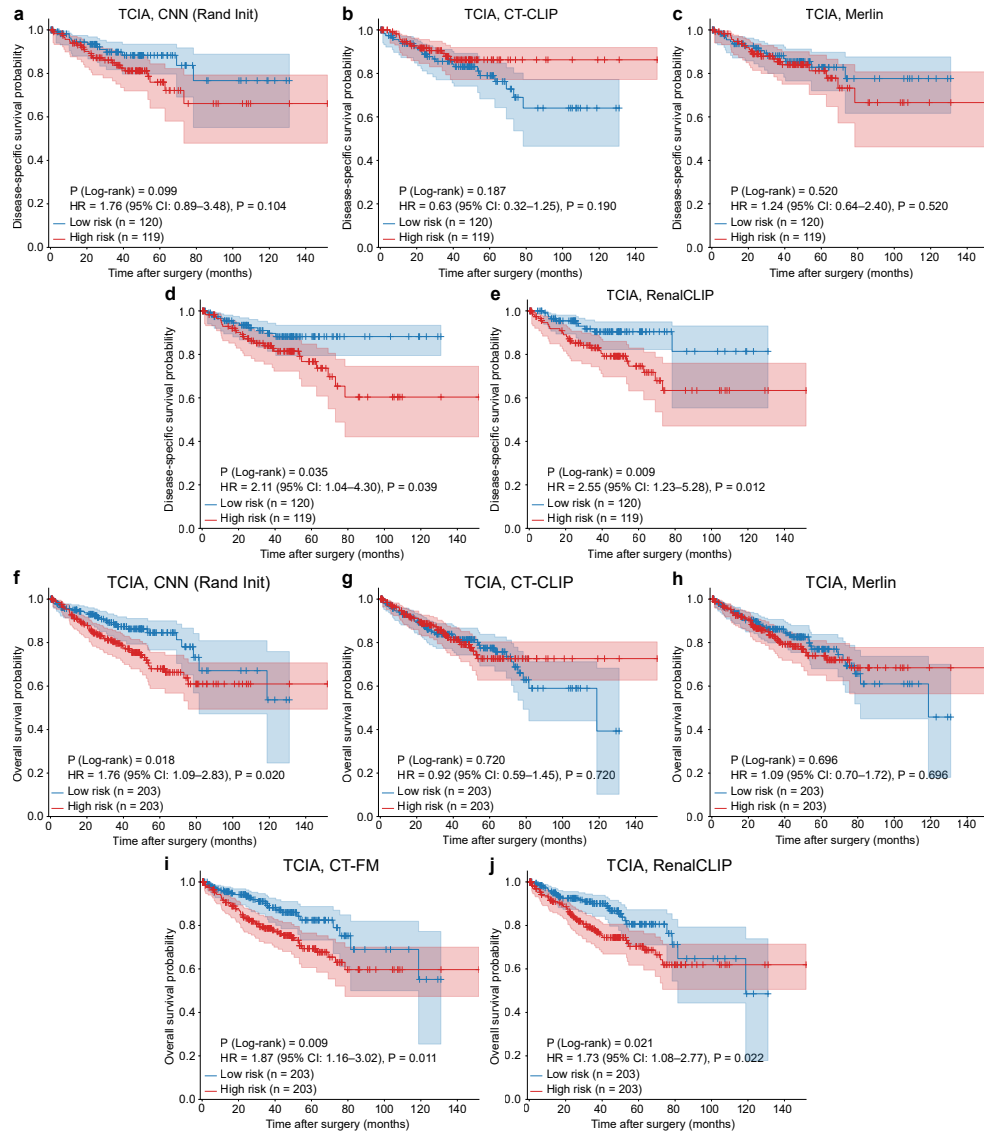
Extended Data Fig. 2 | Extended Data Fig.2 — Evaluation of radiology report generation. **a**, Quantitative performance on four external cohorts, measured by standard language metrics (BLEU-1/-2/-4, METEOR, ROUGE-L). RenalCLIP outperforms all baselines, including generalist 2D vision-language models (GPT-4o, MedGemma) and 3D radiology-specific models (RadFM, CT-CHAT). **b,c**, Qualitative comparison of generated reports from two representative cases. Baseline models exhibit distinct failure modes, including non-specific text generation (RadFM), clinically irrelevant findings due to domain mismatch (CT-CHAT), or factual inaccuracies and omissions (GPT-4o, MedGemma). In contrast, RenalCLIP’s reports demonstrate the best balance of factual accuracy and preservation of critical details. Capped error bars in **a** represent 95% confidence intervals, and the centers of the bars correspond to the computed values of each metric.



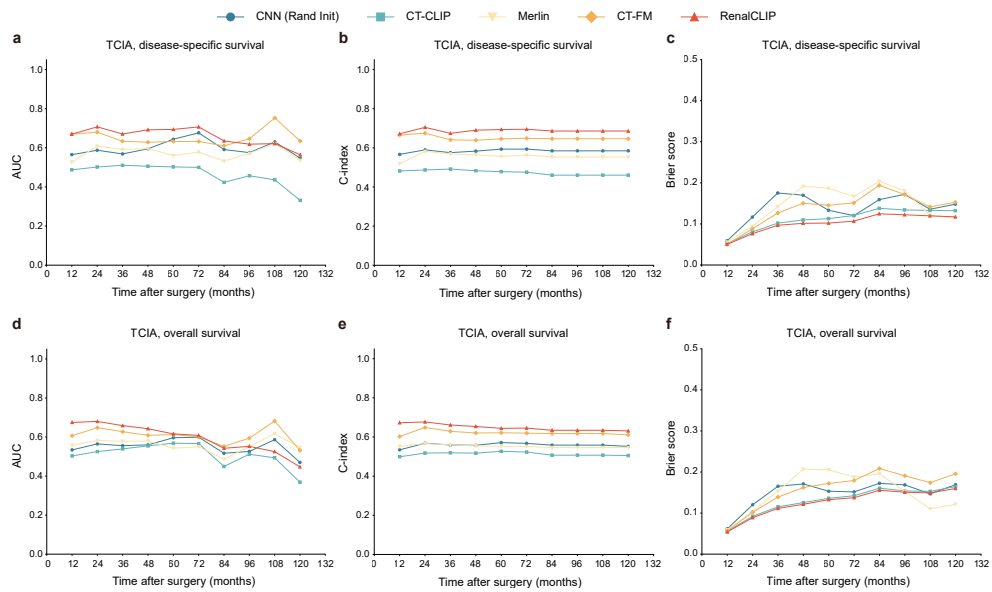
Extended Data Fig. 3 | Supplementary ROC curves for diagnostic performance. Receiver operating characteristic (ROC) curves for the diagnosis of **malignancy** in the TCIA cohort (**a**), and for the diagnosis of **aggressiveness** in the internal validation cohort (**b**), the combined external test cohort (**c**), and the TCIA cohort (**d**). Across all cohorts and tasks shown, RenalCLIP consistently achieves a superior area under the curve (AUC) compared to the baseline models.



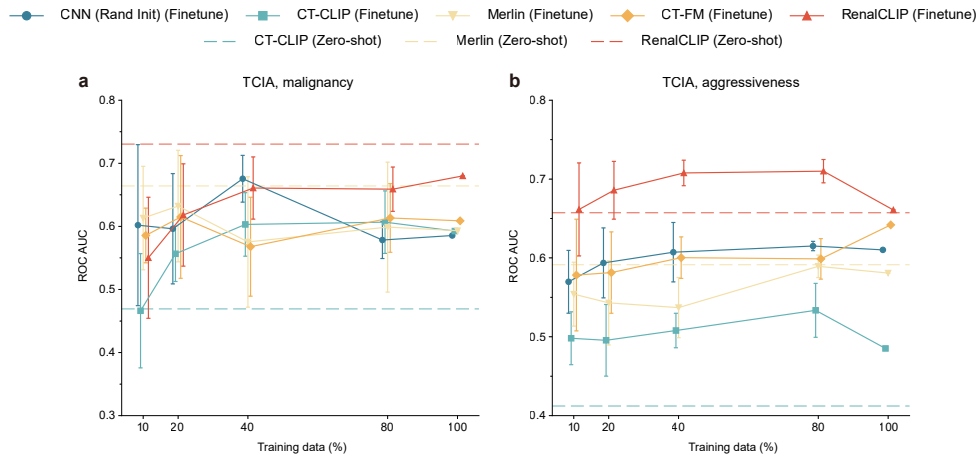
Extended Data Fig. 4 | Supplementary Kaplan-Meier analyses for aggressiveness prediction. **a–e**, Kaplan-Meier curves for recurrence-free survival (RFS) in the internal validation cohort, stratified by the aggressiveness predictions of the four baseline models (**a–d**) and RenalCLIP (**e**). In this less challenging setting, predictions from both RenalCLIP and most baseline models show a statistically significant association with patient outcomes. **f–h**, Kaplan-Meier curves for RFS in the TCIA cohort, stratified by the aggressiveness predictions of the remaining baseline models: CT-CLIP (**f**), Merlin (**g**), and CT-FM (**h**). In stark contrast to the result for RenalCLIP (shown in Fig. 3f), none of these baseline models demonstrate statistically significant prognostic stratification in this challenging external cohort. Hazard ratios (HR) and corresponding p-values were derived from a univariate Cox model; p-values for overall curve comparison were from a two-sided log-rank test. Shaded areas represent 95% confidence intervals.



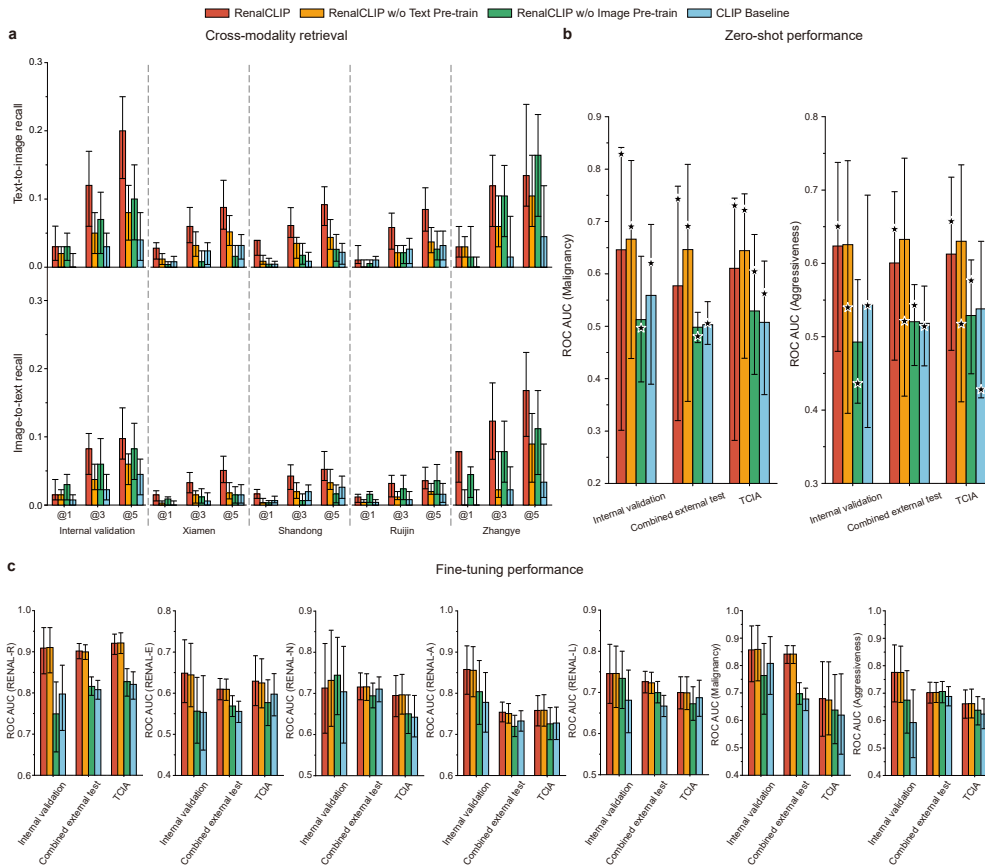
Extended Data Fig. 5 | Supplementary Kaplan-Meier analyses for DSS and OS in the TCIA cohort. **a–e**, Kaplan-Meier curves for disease-specific survival (DSS) in the TCIA cohort, stratified by the prognostic risk scores derived from RenalCLIP and all baseline models. **f–j**, Corresponding Kaplan-Meier curves for overall survival (OS), stratified by the same risk scores. These analyses demonstrate the superior prognostic stratification of RenalCLIP for DSS, and its strong, statistically significant prognostic power for OS. Hazard ratios (HR) and corresponding p-values were derived from a univariate Cox model; p-values for overall curve comparison were from a two-sided log-rank test. Shaded areas represent 95% confidence intervals.



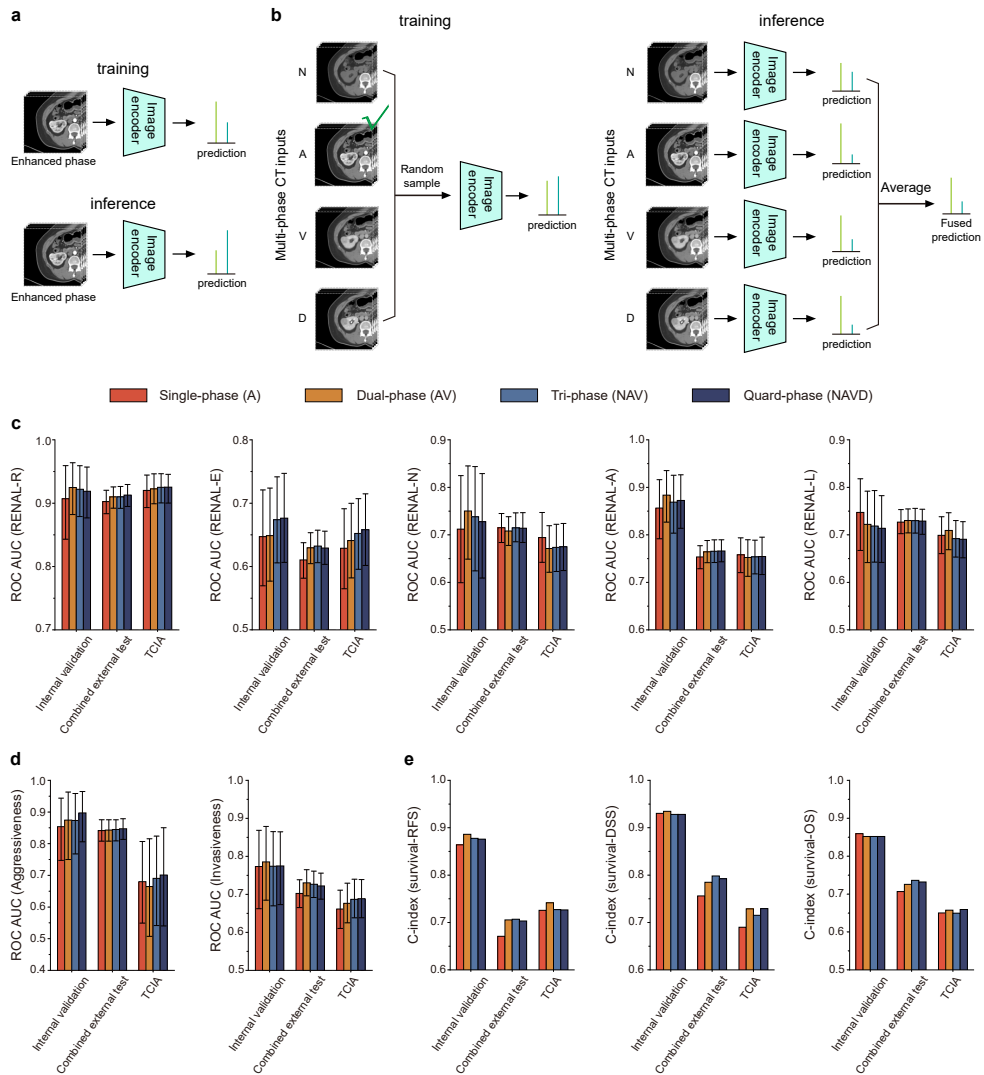
Extended Data Fig. 6 | Supplementary time-dependent prognostic analyses for DSS and OS. Time-dependent prognostic performance for disease-specific survival (DSS; **a–c**) and overall survival (OS; **d–f**) in the TCIA cohort, measured by ROC AUC, C-index, and Brier score. For the C-index for both DSS (**b**) and OS (**e**), and the Brier score for DSS (**c**), RenalCLIP maintains consistent and superior performance over all baseline models across the entire follow-up period. For the remaining metrics—ROC AUC for DSS (**a**) and OS (**d**), and the Brier score for OS (**f**)—RenalCLIP demonstrates superior performance for the majority of the follow-up period (up to 7 years), while remaining highly competitive at later time points.



Extended Data Fig. 7 | Data-efficient fine-tuning and zero-shot performance on the TCIA cohort. Data efficiency curves for malignancy prediction (a) and aggressiveness prediction (b) in the TCIA cohort. The plots show model ROC AUC as a function of the fraction of training data used for fine-tuning, with dashed horizontal lines representing the zero-shot performance of each model. For malignancy prediction (a), RenalCLIP’s zero-shot performance alone surpasses the peak performance of all other models after they were fully fine-tuned on 100% of the data. For the more challenging aggressiveness task (b), RenalCLIP’s zero-shot performance is similarly superior to all fully fine-tuned baseline models, while fine-tuning on RenalCLIP itself yields further performance gains. Data points for training fractions less than 100% represent the mean ROC AUC from five random sampling runs, with capped error bars indicating the standard deviation; the 100% data point represents a single run.



Extended Data Fig. 8 | Ablation study on the contributions of uni-modal pre-training stages. Performance of the full RenalCLIP model is benchmarked against three ablated versions: one without domain-specific text pre-training (w/o Text Pre-train), one without image pre-training (w/o Image Pre-train), and a baseline with no uni-modal pre-training (CLIP Baseline). Models were evaluated across cross-modal retrieval (**a**; top, text-to-image; bottom, image-to-text), zero-shot classification (**b**; left, malignancy; right, aggressiveness), and fine-tuning on key downstream tasks (**c**). The results establish that domain-specific image pre-training provides the most substantial and consistent performance foundation across all tasks. Text pre-training offers a clear synergistic benefit, particularly for cross-modal retrieval and deterministic zero-shot classification. However, a nuanced interaction was observed in stochastic zero-shot classification, where the image-only pre-trained model slightly outperformed the full RenalCLIP model, suggesting that text pre-training may increase sensitivity to prompt variations.



Extended Data Fig. 9 | Ablation study on the multi-phase CT fusion strategy. **a,b**, Schematics of the two data handling strategies. **a**, The standardized single-phase input strategy used for the main experiments, where a single enhanced phase is used. **b**, The late-fusion strategy, where a model trained on randomly sampled single phases is evaluated at inference time by averaging the logits from all available phases. **c–e**, Performance comparison of four cumulative multi-phase input settings. The comparison is shown for R.E.N.A.L. score prediction (**c**), diagnosis (malignancy and aggressiveness) (**d**), and survival prognosis (**e**). The results reveal a nuanced benefit to using multi-phase data: while fusion strategies generally yield a modest performance gain, the single-phase model provides a strong baseline, and no single phase combination is universally optimal across all tasks. Capped error bars in **c** and **d** represent 95% confidence intervals, and the centers of the bars correspond to the computed values of each metric.

Supplementary Data Table 1: R.E.N.A.L. nephrometry score criteria.

Component	Description	Criteria
R	Radius (cm, largest diameter in any single plane)	A. ≤ 4 B. 4–7 C. ≥ 7
E	Exophytic/endophytic (% mass exophytic (protruding out) vs. endophytic (contained) relative to renal parenchyma)	A. $\geq 50\%$ exophytic B. $< 50\%$ exophytic C. 100% endophytic
N	Nearness to collecting system or renal sinus (mm, measure shortest distance)	A. ≥ 7 B. 4–7 C. ≤ 4
A	Anterior/posterior (primary location of tumor relative to coronal plane at level of hilar vessels)	A. Anterior B. Posterior C. Neither
L	Location relative to polar lines	A. Entirely below inferior or above superior pole B. Mass crosses the polar line C. $> 50\%$ of mass lies across the polar line, or is entirely between the polar lines, or crosses the axial midline

Supplementary Data Table 2: ROC AUC on the RENAL-R task across different models and cohorts. Best performing model for each cohort is bolded. 95% CI is included in parentheses.

Cohort	CNN (Rand Init)	CT-CLIP	Merlin	CT-FM	RenalCLIP
Internal validation	0.806 (0.713-0.890)	0.593 (0.506-0.680)	0.838 (0.764-0.906)	0.904 (0.825-0.959)	0.908 (0.848-0.958)
Xiamen	0.788 (0.725-0.847)	0.525 (0.471-0.583)	0.814 (0.760-0.867)	0.883 (0.835-0.930)	0.873 (0.822-0.913)
Shandong	0.836 (0.783-0.886)	0.615 (0.559-0.668)	0.888 (0.843-0.925)	0.922 (0.881-0.955)	0.921 (0.888-0.951)
Ruijin	0.869 (0.823-0.913)	0.651 (0.592-0.709)	0.881 (0.839-0.919)	0.896 (0.856-0.932)	0.935 (0.906-0.961)
Lianyun	0.821 (0.761-0.873)	0.596 (0.538-0.654)	0.829 (0.775-0.880)	0.881 (0.829-0.926)	0.895 (0.850-0.936)
Zhangye	0.778 (0.674-0.868)	0.548 (0.445-0.653)	0.703 (0.600-0.808)	0.868 (0.790-0.934)	0.839 (0.753-0.913)
Combined external test	0.825 (0.801-0.850)	0.587 (0.559-0.613)	0.844 (0.819-0.866)	0.896 (0.877-0.916)	0.902 (0.883-0.920)
TCIA	0.826 (0.789-0.862)	0.559 (0.521-0.600)	0.861 (0.827-0.890)	0.880 (0.850-0.908)	0.920 (0.895-0.945)

Supplementary Data Table 3: ROC AUC on the RENAL-E task across different models and cohorts. Best performing model for each cohort is bolded. 95% CI is included in parentheses.

Cohort	CNN (Rand Init)	CT-CLIP	Merlin	CT-FM	RenalCLIP
Internal validation	0.583 (0.489-0.667)	0.546 (0.456-0.633)	0.502 (0.420-0.581)	0.549 (0.466-0.628)	0.646 (0.573-0.721)
Xiamen	0.562 (0.510-0.614)	0.516 (0.466-0.571)	0.526 (0.471-0.581)	0.570 (0.518-0.623)	0.671 (0.617-0.722)
Shandong	0.576 (0.526-0.627)	0.533 (0.479-0.586)	0.509 (0.457-0.564)	0.537 (0.479-0.590)	0.592 (0.541-0.642)
Ruijin	0.583 (0.528-0.639)	0.528 (0.470-0.587)	0.567 (0.510-0.631)	0.574 (0.518-0.625)	0.578 (0.520-0.635)
Lianyun	0.569 (0.511-0.625)	0.512 (0.457-0.567)	0.525 (0.467-0.585)	0.577 (0.522-0.629)	0.617 (0.561-0.673)
Zhangye	0.487 (0.396-0.598)	0.569 (0.465-0.673)	0.563 (0.443-0.686)	0.594 (0.493-0.706)	0.549 (0.428-0.678)
Combined external test	0.564 (0.538-0.589)	0.519 (0.493-0.546)	0.535 (0.508-0.563)	0.562 (0.536-0.587)	0.610 (0.583-0.637)
TCIA	0.559 (0.508-0.607)	0.541 (0.481-0.599)	0.544 (0.490-0.598)	0.575 (0.525-0.623)	0.629 (0.568-0.686)

Supplementary Data Table 4: ROC AUC on the RENAL-N task across different models and cohorts. Best performing model for each cohort is bolded. 95% CI is included in parentheses.

Cohort	CNN (Rand Init)	CT-CLIP	Merlin	CT-FM	RenalCLIP
Internal validation	0.723 (0.632-0.814)	0.571 (0.455-0.676)	0.544 (0.439-0.656)	0.651 (0.556-0.748)	0.713 (0.600-0.833)
Xiamen	0.614 (0.544-0.692)	0.412 (0.354-0.474)	0.494 (0.413-0.563)	0.681 (0.617-0.753)	0.688 (0.614-0.762)
Shandong	0.613 (0.553-0.672)	0.499 (0.449-0.548)	0.566 (0.504-0.628)	0.670 (0.595-0.742)	0.684 (0.624-0.744)
Ruijin	0.748 (0.680-0.817)	0.535 (0.453-0.614)	0.612 (0.544-0.689)	0.744 (0.663-0.830)	0.743 (0.664-0.825)
Lianyun	0.652 (0.597-0.708)	0.513 (0.452-0.576)	0.574 (0.507-0.646)	0.684 (0.613-0.756)	0.687 (0.623-0.750)
Zhangye	0.796 (0.633-0.932)	0.299 (0.115-0.495)	0.688 (0.448-0.874)	0.779 (0.649-0.896)	0.851 (0.744-0.939)
Combined external test	0.655 (0.625-0.683)	0.490 (0.456-0.518)	0.549 (0.516-0.582)	0.694 (0.660-0.730)	0.715 (0.683-0.747)
TCIA	0.648 (0.594-0.699)	0.494 (0.437-0.547)	0.533 (0.473-0.595)	0.678 (0.632-0.728)	0.694 (0.644-0.742)

Supplementary Data Table 5: ROC AUC on the RENAL-A task across different models and cohorts. Best performing model for each cohort is bolded. 95% CI is included in parentheses.

Cohort	CNN (Rand Init)	CT-CLIP	Merlin	CT-FM	RenalCLIP
Internal validation	0.827 (0.758-0.891)	0.731 (0.658-0.806)	0.725 (0.642-0.805)	0.833 (0.766-0.897)	0.857 (0.796-0.916)
Xiamen	0.767 (0.709-0.825)	0.695 (0.626-0.768)	0.677 (0.606-0.746)	0.779 (0.710-0.844)	0.767 (0.701-0.829)
Shandong	0.755 (0.705-0.801)	0.643 (0.592-0.694)	0.683 (0.636-0.734)	0.785 (0.735-0.833)	0.787 (0.738-0.833)
Ruijin	0.730 (0.678-0.779)	0.724 (0.671-0.771)	0.649 (0.592-0.704)	0.716 (0.661-0.767)	0.712 (0.660-0.768)
Lianyun	0.747 (0.680-0.806)	0.648 (0.582-0.707)	0.611 (0.537-0.686)	0.713 (0.649-0.775)	0.739 (0.668-0.800)
Zhangye	0.725 (0.619-0.818)	0.613 (0.517-0.708)	0.533 (0.428-0.640)	0.768 (0.676-0.849)	0.763 (0.665-0.855)
Combined external test	0.753 (0.727-0.779)	0.674 (0.647-0.699)	0.650 (0.623-0.676)	0.757 (0.731-0.782)	0.754 (0.728-0.778)
TCIA	0.748 (0.709-0.785)	0.707 (0.668-0.741)	0.680 (0.640-0.718)	0.751 (0.715-0.786)	0.758 (0.719-0.796)

Supplementary Data Table 6: ROC AUC on the RENAL-L task across different models and cohorts. Best performing model for each cohort is bolded. 95% CI is included in parentheses.

Cohort	CNN (Rand Init)	CT-CLIP	Merlin	CT-FM	RenalCLIP
Internal validation	0.739 (0.661-0.819)	0.561 (0.467-0.648)	0.677 (0.588-0.755)	0.649 (0.569-0.730)	0.747 (0.668-0.816)
Xiamen	0.597 (0.539-0.661)	0.558 (0.496-0.622)	0.597 (0.531-0.659)	0.601 (0.543-0.663)	0.746 (0.691-0.797)
Shandong	0.654 (0.609-0.701)	0.554 (0.500-0.611)	0.644 (0.591-0.694)	0.666 (0.612-0.719)	0.754 (0.698-0.800)
Ruijin	0.718 (0.658-0.777)	0.492 (0.434-0.552)	0.655 (0.593-0.720)	0.660 (0.598-0.729)	0.698 (0.640-0.757)
Lianyun	0.649 (0.598-0.705)	0.553 (0.494-0.612)	0.597 (0.544-0.656)	0.663 (0.604-0.723)	0.694 (0.644-0.745)
Zhangye	0.597 (0.503-0.691)	0.440 (0.324-0.547)	0.643 (0.519-0.770)	0.561 (0.459-0.676)	0.633 (0.504-0.766)
Combined external test	0.657 (0.632-0.685)	0.525 (0.499-0.552)	0.631 (0.605-0.659)	0.649 (0.621-0.677)	0.727 (0.702-0.751)
TCIA	0.648 (0.608-0.691)	0.529 (0.485-0.577)	0.634 (0.594-0.678)	0.649 (0.604-0.693)	0.699 (0.657-0.739)

Supplementary Data Table 7: Performance of different models on the report generation task for the internal validation cohort. Best performing model for each metric is bolded. 95% CI is included in parentheses.

Metric	RadFM	CT-CHAT	GPT-4o	MedGemma	RenalCLIP
BLEU-1	0.025 (0.020-0.031)	0.148 (0.138-0.159)	0.223 (0.211-0.235)	0.180 (0.166-0.194)	0.297 (0.275-0.319)
BLEU-2	0.014 (0.011-0.017)	0.078 (0.071-0.084)	0.093 (0.085-0.100)	0.082 (0.075-0.090)	0.192 (0.176-0.209)
BLEU-4	0.000 (0.000-0.000)	0.013 (0.009-0.016)	0.020 (0.016-0.024)	0.026 (0.022-0.031)	0.096 (0.083-0.110)
METEOR	0.108 (0.101-0.117)	0.222 (0.214-0.230)	0.248 (0.238-0.258)	0.216 (0.204-0.226)	0.350 (0.333-0.366)
ROUGE-L	0.138 (0.133-0.144)	0.149 (0.142-0.156)	0.185 (0.179-0.191)	0.199 (0.190-0.207)	0.273 (0.259-0.288)

Supplementary Data Table 8: Performance of different models on the report generation task for the Xiamen cohort. Best performing model for each metric is bolded. 95% CI is included in parentheses.

Metric	RadFM	CT-CHAT	GPT-4o	MedGemma	RenalCLIP
BLEU-1	0.015 (0.012-0.017)	0.173 (0.166-0.181)	0.257 (0.249-0.266)	0.176 (0.165-0.187)	0.318 (0.305-0.331)
BLEU-2	0.007 (0.006-0.009)	0.091 (0.087-0.096)	0.112 (0.107-0.117)	0.079 (0.074-0.085)	0.192 (0.183-0.201)
BLEU-4	0.000 (0.000-0.000)	0.020 (0.017-0.022)	0.025 (0.022-0.029)	0.024 (0.021-0.027)	0.076 (0.071-0.081)
METEOR	0.098 (0.094-0.102)	0.212 (0.208-0.218)	0.258 (0.251-0.265)	0.221 (0.213-0.229)	0.334 (0.327-0.341)
ROUGE-L	0.146 (0.141-0.150)	0.153 (0.150-0.157)	0.200 (0.196-0.203)	0.210 (0.205-0.216)	0.267 (0.261-0.275)

Supplementary Data Table 9: Performance of different models on the report generation task for the Shandong cohort. Best performing model for each metric is bolded. 95% CI is included in parentheses.

Metric	RadFM	CT-CHAT	GPT-4o	MedGemma	RenalCLIP
BLEU-1	0.049 (0.044-0.055)	0.095 (0.089-0.100)	0.201 (0.194-0.209)	0.256 (0.246-0.266)	0.226 (0.217-0.236)
BLEU-2	0.027 (0.024-0.030)	0.045 (0.042-0.047)	0.087 (0.083-0.091)	0.109 (0.103-0.115)	0.135 (0.129-0.142)
BLEU-4	0.000 (0.000-0.000)	0.009 (0.007-0.010)	0.019 (0.017-0.021)	0.030 (0.027-0.034)	0.056 (0.052-0.060)
METEOR	0.134 (0.128-0.140)	0.215 (0.210-0.220)	0.301 (0.294-0.307)	0.285 (0.277-0.292)	0.345 (0.338-0.353)
ROUGE-L	0.163 (0.157-0.168)	0.122 (0.119-0.126)	0.195 (0.191-0.198)	0.231 (0.226-0.236)	0.250 (0.244-0.258)

Supplementary Data Table 10: Performance of different models on the report generation task for the Ruijin cohort. Best performing model for each metric is bolded. 95% CI is included in parentheses.

Metric	RadFM	CT-CHAT	GPT-4o	MedGemma	RenalCLIP
BLEU-1	0.029 (0.024-0.034)	0.154 (0.146-0.162)	0.226 (0.217-0.236)	0.207 (0.194-0.220)	0.279 (0.266-0.292)
BLEU-2	0.016 (0.013-0.019)	0.086 (0.081-0.091)	0.096 (0.090-0.102)	0.089 (0.082-0.095)	0.167 (0.159-0.176)
BLEU-4	0.000 (0.000-0.000)	0.022 (0.019-0.024)	0.020 (0.016-0.023)	0.028 (0.024-0.032)	0.068 (0.064-0.074)
METEOR	0.119 (0.113-0.125)	0.230 (0.224-0.235)	0.271 (0.264-0.278)	0.240 (0.232-0.249)	0.342 (0.333-0.350)
ROUGE-L	0.169 (0.163-0.175)	0.155 (0.150-0.159)	0.192 (0.189-0.196)	0.211 (0.205-0.215)	0.263 (0.255-0.270)

Supplementary Data Table 11: Performance of different models on the report generation task for the Zhangye cohort. Best performing model for each metric is bolded. 95% CI is included in parentheses.

Metric	RadFM	CT-CHAT	GPT-4o	MedGemma	RenalCLIP
BLEU-1	0.005 (0.003-0.009)	0.172 (0.155-0.190)	0.265 (0.245-0.283)	0.149 (0.123-0.175)	0.343 (0.313-0.352)
BLEU-2	0.003 (0.002-0.005)	0.084 (0.074-0.095)	0.120 (0.110-0.130)	0.067 (0.056-0.079)	0.199 (0.180-0.205)
BLEU-4	0.000 (0.000-0.000)	0.018 (0.014-0.022)	0.027 (0.021-0.032)	0.018 (0.014-0.023)	0.076 (0.066-0.082)
METEOR	0.095 (0.079-0.113)	0.193 (0.184-0.204)	0.241 (0.227-0.257)	0.210 (0.192-0.229)	0.291 (0.276-0.305)
ROUGE-L	0.132 (0.121-0.143)	0.146 (0.138-0.154)	0.189 (0.181-0.198)	0.193 (0.185-0.202)	0.238 (0.227-0.249)

Supplementary Data Table 12: ROC AUC on the malignancy diagnosis task across different models and cohorts. Best performing model for each cohort is bolded. 95% CI is included in parentheses.

Cohort	CNN (Rand Init)	CT-CLIP	Merlin	CT-FM	RenalCLIP
Internal validation	0.791 (0.662-0.894)	0.616 (0.453-0.769)	0.733 (0.561-0.878)	0.732 (0.561-0.886)	0.856 (0.741-0.944)
Xiamen	0.736 (0.662-0.805)	0.682 (0.606-0.753)	0.599 (0.526-0.670)	0.751 (0.684-0.812)	0.890 (0.840-0.934)
Shandong	0.707 (0.621-0.791)	0.597 (0.482-0.696)	0.704 (0.593-0.806)	0.738 (0.630-0.831)	0.738 (0.631-0.835)
Ruijin	0.685 (0.591-0.774)	0.611 (0.521-0.708)	0.718 (0.626-0.809)	0.682 (0.583-0.785)	0.824 (0.726-0.908)
Lianyun	0.693 (0.604-0.783)	0.566 (0.474-0.655)	0.619 (0.538-0.700)	0.738 (0.647-0.819)	0.838 (0.765-0.902)
Zhangye	0.738 (0.584-0.865)	0.326 (0.172-0.496)	0.507 (0.308-0.702)	0.719 (0.560-0.863)	0.880 (0.719-0.982)
Combined external test	0.717 (0.676-0.756)	0.600 (0.555-0.638)	0.650 (0.607-0.690)	0.739 (0.698-0.779)	0.841 (0.808-0.873)
TCIA	0.586 (0.453-0.734)	0.593 (0.430-0.733)	0.593 (0.437-0.739)	0.609 (0.455-0.755)	0.680 (0.542-0.814)

Supplementary Data Table 13: ROC AUC on the aggressiveness diagnosis task across different models and cohorts. Best performing model for each cohort is bolded. 95% CI is included in parentheses.

Cohort	CNN (Rand Init)	CT-CLIP	Merlin	CT-FM	RenalCLIP
Internal validation	0.592 (0.466-0.713)	0.490 (0.356-0.619)	0.584 (0.440-0.717)	0.668 (0.544-0.782)	0.775 (0.673-0.878)
Xiamen	0.751 (0.655-0.841)	0.586 (0.467-0.694)	0.644 (0.521-0.767)	0.817 (0.759-0.869)	0.817 (0.738-0.888)
Shandong	0.653 (0.582-0.725)	0.556 (0.481-0.634)	0.661 (0.577-0.737)	0.646 (0.570-0.723)	0.707 (0.639-0.775)
Ruijin	0.650 (0.572-0.728)	0.535 (0.464-0.611)	0.643 (0.570-0.713)	0.649 (0.573-0.719)	0.654 (0.581-0.724)
Lianyun	0.651 (0.546-0.746)	0.543 (0.421-0.653)	0.740 (0.644-0.840)	0.636 (0.520-0.732)	0.645 (0.532-0.756)
Zhangye	0.541 (0.393-0.683)	0.513 (0.376-0.656)	0.413 (0.267-0.557)	0.345 (0.214-0.484)	0.484 (0.358-0.631)
Combined external test	0.676 (0.639-0.712)	0.547 (0.508-0.588)	0.681 (0.642-0.719)	0.680 (0.640-0.716)	0.703 (0.667-0.738)
TCIA	0.610 (0.559-0.661)	0.485 (0.434-0.539)	0.581 (0.527-0.633)	0.642 (0.589-0.696)	0.661 (0.611-0.708)

Supplementary Data Table 14: C-index on the prognosis (RFS endpoint) task across different models and cohorts. Best performing model for each cohort is bolded.

Cohort	CNN (Rand Init)	CT-CLIP	Merlin	CT-FM	RenalCLIP
Internal validation	0.684	0.509	0.711	0.709	0.864
Xiamen	0.668	0.760	0.641	0.519	0.828
Ruijin	0.456	0.529	0.538	0.609	0.523
Zhangye	0.794	0.420	0.605	0.726	0.741
Combined external test	0.640	0.511	0.583	0.661	0.671
TCIA	0.547	0.461	0.535	0.592	0.726

Supplementary Data Table 15: C-index on the prognosis (DSS endpoint) task across different models and cohorts. Best performing model for each cohort is bolded.

Cohort	CNN (Rand Init)	CT-CLIP	Merlin	CT-FM	RenalCLIP
Internal validation	0.702	0.580	0.754	0.765	0.930
Xiamen	0.804	0.754	0.862	0.919	0.873
Ruijin	0.663	0.587	0.634	0.708	0.700
Zhangye	0.780	0.421	0.572	0.694	0.720
Combined external test	0.738	0.527	0.654	0.742	0.756
TCIA	0.586	0.475	0.561	0.649	0.690

Supplementary Data Table 16: C-index on the prognosis OS endpoint) task across different models and cohorts. Best performing model for each cohort is bolded.

Cohort	CNN (Rand Init)	CT-CLIP	Merlin	CT-FM	RenalCLIP
Internal validation	0.682	0.576	0.641	0.704	0.859
Xiamen	0.797	0.803	0.872	0.763	0.691
Ruijin	0.645	0.537	0.629	0.635	0.648
Zhangye	0.780	0.421	0.572	0.694	0.720
Combined external test	0.724	0.515	0.646	0.690	0.707
TCIA	0.564	0.517	0.553	0.623	0.650

Supplementary Data Table 17: Univariate and multivariate analysis of recurrence-free survival in TCIA cohort.

Variables	Univariate analysis			Multivariate analysis		
	Hazard Ratio	95%CI	p-value	Hazard Ratio	95%CI	p-value
CNN (Rand Init)						
TNM Stage						
Stage II vs Stage I	2.80	0.79-9.96	0.111	2.39	0.64-8.90	0.193
Stage III vs Stage I	10.09	4.09-24.9	< 0.001*	9.67	3.86-24.2	< 0.001*
Stage IV vs Stage I	40.14	16.07-100.23	< 0.001*	30.57	11.60-80.52	< 0.001*
WHO/ISUP Grade						
Grade 2 vs Grade 1	0.60	0.08-4.59	0.623	0.558	0.07-4.36	0.578
Grade 3 vs Grade 1	1.63	0.22-12.02	0.635	0.936	0.12-7.08	0.949
Grade 4 vs Grade 1	4.43	0.69-33.46	0.149	1.893	0.24-15.22	0.548
Risk score	1.04	0.95-1.14	0.360	0.956	0.87-1.05	0.371
CT-CLIP						
TNM Stage						
Stage II vs Stage I	2.80	0.79-9.96	0.111	2.20	0.60-8.02	0.234
Stage III vs Stage I	10.09	4.09-24.9	< 0.001*	9.22	3.70-22.95	< 0.001*
Stage IV vs Stage I	40.14	16.07-100.23	< 0.001*	28.05	10.76-73.14	< 0.001*
WHO/ISUP Grade						
Grade 2 vs Grade 1	0.60	0.08-4.59	0.623	0.49	0.06-3.81	0.497
Grade 3 vs Grade 1	1.63	0.22-12.02	0.635	0.87	0.11-6.59	0.891
Grade 4 vs Grade 1	4.43	0.69-33.46	0.149	1.61	0.20-12.75	0.653
Risk score	0.76	0.36-1.59	0.464	0.869	0.41-1.85	0.717
Merlin						
TNM Stage						
Stage II vs Stage I	2.80	0.79-9.96	0.111	2.04	0.55-7.53	0.283
Stage III vs Stage I	10.09	4.09-24.9	< 0.001*	8.72	3.49-21.81	< 0.001*
Stage IV vs Stage I	40.14	16.07-100.23	< 0.001*	29.01	11.12-75.72	< 0.001*
WHO/ISUP Grade						
Grade 2 vs Grade 1	0.60	0.08-4.59	0.623	0.55	0.07-4.26	0.564
Grade 3 vs Grade 1	1.63	0.22-12.02	0.635	0.95	0.13-7.23	0.963
Grade 4 vs Grade 1	4.43	0.69-33.46	0.149	1.76	0.22-14.00	0.592
Risk score	1.02	0.97-1.07	0.408	1.02	0.97-1.06	0.436

P-values were calculated using the Wald test. Asterisk (*) indicates statistical significance ($p < 0.05$).

Supplementary Data Table 18: Univariate and multivariate analysis of recurrence-free survival in TCIA cohort. continued.

Variables	Univariate analysis			Multivariate analysis		
	Hazard Ratio	95%CI	p-value	Hazard Ratio	95%CI	p-value
CT-FM						
TNM Stage						
Stage II vs Stage I	2.80	0.79-9.96	0.111	2.15	0.58-7.98	0.251
Stage III vs Stage I	10.09	4.09-24.9	< 0.001*	9.06	3.58-22.92	< 0.001*
Stage IV vs Stage I	40.14	16.07-100.23	< 0.001*	28.33	10.84-74.03	< 0.001*
WHO/ISUP Grade						
Grade 2 vs Grade 1	0.60	0.08-4.59	0.623	0.50	0.06-4.05	0.515
Grade 3 vs Grade 1	1.63	0.22-12.02	0.635	0.89	0.11-6.87	0.908
Grade 4 vs Grade 1	4.43	0.69-33.46	0.149	1.62	0.18-14.37	0.664
Risk score	1.058	1.02-1.10	0.007*	1.00	0.96-1.05	0.969
RenalCLIP						
TNM Stage						
Stage II vs Stage I	2.80	0.79-9.96	0.111	1.23	0.32-4.78	0.765
Stage III vs Stage I	10.09	4.09-24.9	< 0.001*	5.90	2.23-15.65	< 0.001*
Stage IV vs Stage I	40.14	16.07-100.23	< 0.001*	22.13	8.27-59.28	< 0.001*
WHO/ISUP Grade						
Grade 2 vs Grade 1	0.60	0.08-4.59	0.623	0.45	0.06-3.50	0.445
Grade 3 vs Grade 1	1.63	0.22-12.02	0.635	0.81	0.11-6.10	0.836
Grade 4 vs Grade 1	4.43	0.69-33.46	0.149	1.14	0.14-9.22	0.904
Risk score	4.31	2.46-7.54	< 0.001*	2.27	1.17-4.42	0.016*

P-values were calculated using the Wald test. Asterisk (*) indicates statistical significance ($p < 0.05$).

Supplementary Data Table 19: Performance of different models on the cross-modal retrieval task for the internal validation cohort. Best performing model for each metric is bolded. 95% CI is included in parentheses.

Metric	CT-CLIP	Merlin	RenalCLIP
Text-to-image			
Recall@1	0.000 (0.000-0.000)	0.020 (0.000-0.040)	0.030 (0.010-0.060)
Recall@3	0.000 (0.000-0.010)	0.060 (0.020-0.090)	0.120 (0.060-0.170)
Recall@5	0.000 (0.000-0.030)	0.090 (0.040-0.120)	0.200 (0.130-0.250)
Image-to-text			
Recall@1	0.010 (0.000-0.010)	0.020 (0.010-0.030)	0.020 (0.010-0.050)
Recall@3	0.010 (0.000-0.030)	0.040 (0.010-0.070)	0.110 (0.060-0.140)
Recall@5	0.010 (0.000-0.030)	0.050 (0.020-0.090)	0.130 (0.090-0.190)

Supplementary Data Table 20: Performance of different models on the cross-modal retrieval task for the Xiamen cohort. Best performing model for each metric is bolded. 95% CI is included in parentheses.

Metric	CT-CLIP	Merlin	RenalCLIP
Text-to-image			
Recall@1	0.000 (0.000-0.000)	0.004 (0.000-0.012)	0.028 (0.012-0.036)
Recall@3	0.000 (0.000-0.004)	0.016 (0.004-0.028)	0.060 (0.036-0.088)
Recall@5	0.000 (0.000-0.012)	0.024 (0.008-0.036)	0.088 (0.056-0.127)
Image-to-text			
Recall@1	0.000 (0.000-0.004)	0.012 (0.000-0.016)	0.020 (0.008-0.028)
Recall@3	0.004 (0.000-0.008)	0.020 (0.008-0.032)	0.044 (0.024-0.064)
Recall@5	0.004 (0.000-0.012)	0.024 (0.012-0.044)	0.068 (0.044-0.096)

Supplementary Data Table 21: Performance of different models on the cross-modal retrieval task for the Shandong cohort. Best performing model for each metric is bolded. 95% CI is included in parentheses.

Metric	CT-CLIP	Merlin	RenalCLIP
Text-to-image			
Recall@1	0.000 (0.000-0.004)	0.004 (0.000-0.009)	0.039 (0.017-0.039)
Recall@3	0.000 (0.000-0.009)	0.017 (0.004-0.026)	0.061 (0.044-0.087)
Recall@5	0.004 (0.000-0.013)	0.022 (0.013-0.039)	0.092 (0.061-0.118)
Image-to-text			
Recall@1	0.000 (0.000-0.004)	0.000 (0.000-0.004)	0.022 (0.013-0.031)
Recall@3	0.004 (0.000-0.013)	0.004 (0.000-0.017)	0.057 (0.031-0.079)
Recall@5	0.004 (0.000-0.013)	0.013 (0.000-0.031)	0.070 (0.048-0.105)

Supplementary Data Table 22: Performance of different models on the cross-modal retrieval task for the Ruijin cohort. Best performing model for each metric is bolded. 95% CI is included in parentheses.

Metric	CT-CLIP	Merlin	RenalCLIP
Text-to-image			
Recall@1	0.000 (0.000-0.000)	0.005 (0.000-0.011)	0.011 (0.005-0.032)
Recall@3	0.000 (0.000-0.000)	0.021 (0.005-0.032)	0.058 (0.026-0.079)
Recall@5	0.000 (0.000-0.005)	0.032 (0.011-0.048)	0.085 (0.053-0.116)
Image-to-text			
Recall@1	0.000 (0.000-0.000)	0.005 (0.000-0.011)	0.016 (0.005-0.021)
Recall@3	0.000 (0.000-0.000)	0.011 (0.000-0.021)	0.042 (0.016-0.058)
Recall@5	0.000 (0.000-0.000)	0.016 (0.005-0.032)	0.048 (0.032-0.074)

Supplementary Data Table 23: Performance of different models on the cross-modal retrieval task for the Zhangye cohort. Best performing model for each metric is bolded. 95% CI is included in parentheses.

Metric	CT-CLIP	Merlin	RenalCLIP
Text-to-image			
Recall@1	0.015 (0.000-0.015)	0.030 (0.000-0.045)	0.030 (0.015-0.060)
Recall@3	0.015 (0.000-0.045)	0.045 (0.015-0.090)	0.119 (0.060-0.164)
Recall@5	0.015 (0.000-0.060)	0.090 (0.045-0.134)	0.134 (0.090-0.239)
Image-to-text			
Recall@1	0.000 (0.000-0.000)	0.015 (0.000-0.015)	0.104 (0.045-0.104)
Recall@3	0.000 (0.000-0.030)	0.030 (0.015-0.075)	0.164 (0.090-0.239)
Recall@5	0.015 (0.000-0.030)	0.075 (0.030-0.134)	0.224 (0.134-0.299)

Supplementary Data Table 24: Generic prompt templates for zero-shot classification. This table lists the 20 generic sentence templates used to construct the full prompt ensemble. To generate a complete prompt, the {} placeholder within each template is populated with a specific class descriptor. The full sets of class descriptors for the malignancy and aggressiveness tasks are detailed in Supplementary Data Tables [25-26](#)

A soft tissue mass that is {} is visible in the kidney.
A density shadow that is {} is observed in the kidney.
An area that is {} is visualized at the pole of the kidney.
A mass-like shadow that is {} is noted in the kidney.
An occupying lesion that is {} is seen in the kidney.
An abnormality that is {} is detected in the kidney.
A region of interest that is {} is found in the kidney.
A structural irregularity that is {} is visible in the kidney.
A mixed-density lesion that is {} is apparent in the kidney.
A nodule that is {} is observed in the kidney.
A shadow-like lesion that is {} is identified in the kidney.
A well-defined region that is {} is noted in the kidney.
An abnormal soft tissue that is {} is detected in the kidney.
A feature that is {} is recognized in the kidney.
A density lesion that is {} is revealed in the kidney.
The kidney shows a soft tissue mass that is {}.
The kidney reveals a density shadow that is {}.
The kidney demonstrates a lesion that is {}.
The kidney presents an occupying abnormality that is {}.
The kidney displays a structural irregularity that is {}.

Supplementary Data Table 25: Representative text prompts for malignancy zero-shot classification.

Task	Class	Representative Class Prompts
Malignancy	Benign	benign, described as a mass containing fatty soft tissue, consistent with an angiomyolipoma
		benign, presenting as a round cystic lesion with a clear boundary and no enhancement after contrast
		benign, a finding of a nodule with uniform density, smooth borders, and no significant enhancement
		benign, a complex cyst with fine septa showing only mild, non-suspicious enhancement
	Malignant	benign, a lesion showing mild and uniform progressive enhancement after contrast, without washout
		malignant, showing early significant uneven enhancement during the corticomedullary phase, and reduced density in the nephrographic phase
		malignant, presenting as a mass-like abnormal density shadow which is uneven and contains a central necrotic area
		malignant, a cystic-solid occupying lesion with thickened, irregular walls and enhancing solid nodules
		malignant, described as a solid tumor showing rapid enhancement and subsequent washout of contrast
		malignant, an irregular mass with unclear boundaries and heterogeneous density

Supplementary Data Table 26: Representative text prompts for aggressiveness zero-shot classification.

Task	Class	Representative Class Prompts
Aggressiveness	Indolent	non-invasive, as the lesion is confined by the renal capsule and has not breached it
		non-invasive, with the perirenal fat spaces appearing clear and uninvolved
		non-invasive, showing no signs of involvement of the renal pelvis or calyces
		non-invasive, with no evidence of tumor thrombus in the renal vein or inferior vena cava
		non-invasive, presenting as a well-circumscribed lesion with sharp, distinct borders
	Aggressive	invasive, as the tumor demonstrates extrarenal extension into the perirenal fat
		invasive, as the tumor appears to have breached the renal capsule
		invasive, showing clear infiltration of the renal pelvis or collecting system
		invasive, with a filling defect consistent with a tumor thrombus in the renal vein or IVC
		invasive, presenting as an infiltrative mass with poorly defined or blurred borders

Supplementary Data Table 27: ROC AUC on the zero-shot malignancy diagnosis task across different models and cohorts. Results are grouped by zero-shot strategy. Best performing model for each cohort is bolded. 95% CI is included in parentheses.

Cohort	CT-CLIP	Merlin	RenalCLIP
Stochastic prompt sampling			
Internal validation	0.493 (0.439-0.542)	0.569 (0.439-0.684)	0.646 (0.302-0.841)
Combined external test	0.566 (0.524-0.590)	0.486 (0.400-0.568)	0.577 (0.320-0.768)
TCIA	0.518 (0.423-0.629)	0.660 (0.521-0.729)	0.611 (0.282-0.745)
Maximum similarity ensemble			
Internal validation	0.449	0.656	0.829
Combined external test	0.570	0.464	0.743
TCIA	0.469	0.664	0.730

Supplementary Data Table 28: ROC AUC on the zero-shot aggressiveness diagnosis task across different models and cohorts. Results are grouped by zero-shot strategy. Best performing model for each cohort is bolded. 95% CI is included in parentheses.

Cohort	CT-CLIP	Merlin	RenalCLIP
Stochastic prompt sampling			
Internal validation	0.489 (0.462-0.522)	0.548 (0.491-0.602)	0.624 (0.480-0.738)
Combined external test	0.477 (0.448-0.505)	0.567 (0.505-0.624)	0.601 (0.468-0.698)
TCIA	0.425 (0.406-0.457)	0.580 (0.534-0.607)	0.613 (0.481-0.718)
Maximum similarity ensemble			
Internal validation	0.483	0.514	0.650
Combined external test	0.480	0.588	0.647
TCIA	0.412	0.591	0.657

Supplementary Data Table 29: Model performance on malignancy diagnosis with varying proportions of training data. All values represent ROC AUC. For training data proportions less than 1.0, values are the mean \pm standard deviation of $n = 5$ independent runs with different random seeds. The 1.0 proportion represents a single run on the full training dataset. The best-performing model for each cohort and proportion is highlighted in bold.

Cohort	CNN (Rand Init)	CT-CLIP	Merlin	CT-FM	RenalCLIP
10% Training data					
Internal validation	0.546 \pm 0.042	0.507 \pm 0.096	0.615 \pm 0.044	0.550 \pm 0.104	0.613 \pm 0.069
Combined external test	0.560 \pm 0.034	0.505 \pm 0.027	0.527 \pm 0.023	0.585 \pm 0.028	0.668 \pm 0.061
TCIA	0.602 \pm 0.128	0.466 \pm 0.091	0.613 \pm 0.082	0.586 \pm 0.043	0.550 \pm 0.096
20% Training data					
Internal validation	0.628 \pm 0.073	0.615 \pm 0.070	0.688 \pm 0.063	0.687 \pm 0.082	0.729 \pm 0.048
Combined external test	0.633 \pm 0.030	0.547 \pm 0.024	0.566 \pm 0.034	0.637 \pm 0.043	0.747 \pm 0.081
TCIA	0.596 \pm 0.087	0.557 \pm 0.044	0.632 \pm 0.088	0.615 \pm 0.097	0.618 \pm 0.081
40% Training data					
Internal validation	0.691 \pm 0.078	0.657 \pm 0.036	0.644 \pm 0.096	0.730 \pm 0.083	0.776 \pm 0.028
Combined external test	0.667 \pm 0.026	0.583 \pm 0.029	0.605 \pm 0.017	0.691 \pm 0.043	0.800 \pm 0.039
TCIA	0.676 \pm 0.037	0.603 \pm 0.050	0.575 \pm 0.103	0.568 \pm 0.078	0.661 \pm 0.049
80% Training data					
Internal validation	0.771 \pm 0.050	0.654 \pm 0.050	0.694 \pm 0.028	0.756 \pm 0.037	0.779 \pm 0.033
Combined external test	0.711 \pm 0.010	0.598 \pm 0.012	0.632 \pm 0.015	0.728 \pm 0.015	0.829 \pm 0.011
TCIA	0.578 \pm 0.029	0.607 \pm 0.049	0.599 \pm 0.103	0.613 \pm 0.054	0.659 \pm 0.035
100% Training data					
Internal validation	0.791	0.616	0.733	0.732	0.856
Combined external test	0.717	0.600	0.650	0.739	0.841
TCIA	0.586	0.593	0.593	0.609	0.680

Supplementary Data Table 30: Model performance on aggressiveness diagnosis with varying proportions of training data. All values represent ROC AUC. For training data proportions less than 1.0, values are the mean \pm standard deviation of $n = 5$ independent runs with different random seeds. The 1.0 proportion represents a single run on the full training dataset. The best-performing model for each cohort and proportion is highlighted in bold.

Cohort	CNN (Rand Init)	CT-CLIP	Merlin	CT-FM	RenalCLIP
10% Training data					
Internal validation	0.580 \pm 0.015	0.482 \pm 0.068	0.552 \pm 0.040	0.636 \pm 0.075	0.686 \pm 0.043
Combined external test	0.618 \pm 0.034	0.509 \pm 0.050	0.578 \pm 0.053	0.610 \pm 0.087	0.672 \pm 0.043
TCIA	0.570 \pm 0.040	0.498 \pm 0.034	0.554 \pm 0.041	0.578 \pm 0.071	0.661 \pm 0.059
20% Training data					
Internal validation	0.601 \pm 0.044	0.481 \pm 0.059	0.558 \pm 0.074	0.644 \pm 0.058	0.706 \pm 0.046
Combined external test	0.641 \pm 0.022	0.532 \pm 0.023	0.592 \pm 0.041	0.645 \pm 0.045	0.702 \pm 0.032
TCIA	0.594 \pm 0.044	0.496 \pm 0.045	0.543 \pm 0.053	0.581 \pm 0.052	0.686 \pm 0.037
40% Training data					
Internal validation	0.606 \pm 0.035	0.462 \pm 0.093	0.578 \pm 0.037	0.696 \pm 0.025	0.720 \pm 0.031
Combined external test	0.660 \pm 0.030	0.522 \pm 0.022	0.650 \pm 0.038	0.673 \pm 0.027	0.719 \pm 0.032
TCIA	0.607 \pm 0.038	0.508 \pm 0.022	0.537 \pm 0.038	0.600 \pm 0.026	0.708 \pm 0.016
80% Training data					
Internal validation	0.605 \pm 0.034	0.468 \pm 0.054	0.598 \pm 0.037	0.700 \pm 0.021	0.751 \pm 0.011
Combined external test	0.694 \pm 0.009	0.534 \pm 0.022	0.686 \pm 0.017	0.690 \pm 0.012	0.734 \pm 0.013
TCIA	0.615 \pm 0.006	0.534 \pm 0.034	0.589 \pm 0.014	0.599 \pm 0.026	0.710 \pm 0.015
100% Training data					
Internal validation	0.592	0.490	0.584	0.668	0.775
Combined external test	0.676	0.547	0.681	0.680	0.703
TCIA	0.610	0.485	0.581	0.642	0.661

Supplementary Data Table 31: LLM prompt for kidney-specific report extraction.

Context

You are a radiologist tasked with extracting information from radiology reports. The report you will be given is for a contrast-enhanced abdominal CT. Your task is to separately extract the descriptive findings pertaining to the left kidney and the right kidney. Ensure that descriptions from all contrast phases are included. If there are any descriptions pertaining to both kidneys (i.e., bilateral findings), extract this information and appropriately place it in the fields for both the left and right kidneys. The output must be in JSON format.

Example

Input:

Report Findings:

Liver surface is smooth, lobes are proportional, and liver parenchyma shows no abnormal density; Spleen is not enlarged, with uniform density; Pancreas is unremarkable. A punctate high-density focus is seen in the right kidney. A small, low-density nodule measuring approximately 11x8mm is seen at the lower pole of the left kidney, protruding from the renal surface. It shows slight enhancement after contrast administration, with heterogeneous density and an internal low-density area. Multiple tiny cystic non-enhancing foci are also seen in the left kidney; The medial limb and root of the left adrenal gland are slightly thickened; No free fluid in the abdominal cavity.

Impression:

Nodule at the lower pole of the left kidney, likely a benign lesion, MRI recommended if necessary; Small cysts in the left kidney; Small stone in the right kidney.

JSON Output:

```
{
  "report_findings": {
    "left_kidney": "A small, low-density nodule measuring approximately 11x8mm is seen at the lower pole of the left kidney, protruding from the renal surface. It shows slight enhancement after contrast administration, with heterogeneous density and an internal low-density area. Multiple tiny cystic non-enhancing foci are also seen in the left kidney; The medial limb and root of the left adrenal gland are slightly thickened;",
    "right_kidney": "A punctate high-density focus is seen in the right kidney"
  },
  "impression": {
    "left_kidney": "Nodule at the lower pole of the left kidney, likely a benign lesion, MRI recommended if necessary; Small cysts in the left kidney;",
    "right_kidney": "Small stone in the right kidney."
  }
}
```

Your Turn

Input:

Report Findings: {}

Impression: {}

Output:

Supplementary Data Table 32: LLM prompt for report translation.

```
# Task  
Accurately translate the following imaging report findings and impression into English. The  
output must be in JSON format.  
  
# Input  
{  
  
# Output
```

Supplementary Data Table 33: Questionnaire for LLM-based renal mass feature extraction.

No.	Questions	Options
1.	Overall Nature and Number of Lesions	A. Solitary lesion B. Multiple/Disseminated lesions C. Other D. Not mentioned/No mass
2.	Location of the Renal Mass	A. Upper pole B. Mid pole C. Lower pole D. Not mentioned/No mass
3.	Size of the Renal Mass (assessed by maximum transverse diameter)	A. ≤ 4 cm B. > 4 cm and ≤ 7 cm C. > 7 cm and ≤ 10 cm D. > 10 cm E. Not mentioned/No mass
4.	Exophytic Renal Mass?	A. Yes B. Not described
5.	Morphology of the Renal Mass?	A. Round, ovoid, or oval-shaped B. Irregular, ill-defined C. Mass-like D. Lobulated E. Not mentioned/No mass
6.	Cystic or Solid Nature of the Renal Mass?	A. Cystic B. Cystic and solid C. Solid D. Not mentioned/No mass
7.	Density/Signal Intensity of the Renal Mass?	A. Hypodense/Low signal B. Isodense/Isointense C. Hyperdense/High signal D. Heterogeneous density/signal E. Fat density (Angiomyolipoma (AML)) F. Mixed density G. Not mentioned/No mass

Supplementary Data Table 34: Questionnaire for LLM-based renal mass feature extraction. Continued.

No.	Questions	Options
8.	Imaging Evidence of Necrosis within the Renal Mass?	A. Yes B. No C. Not mentioned/No mass
9.	Enhancement Pattern of the Renal Mass after Contrast Administration?	A. Non-enhancing B. Mild enhancement, apparent enhancement C. Moderate enhancement D. Marked enhancement E. Heterogeneous enhancement F. Cyst wall/septal enhancement G. Not mentioned/No mass
10.	Enhancement of the Renal Mass during the Arterial Phase?	A. No enhancement B. Mild enhancement C. Marked enhancement D. Not mentioned/No mass
11.	Clarity of Renal Mass Margins?	A. Well-defined (clear margins) B. Ill-defined (poorly defined margins) C. Not mentioned/No mass
12.	Is the Renal Mass Likely Benign or Malignant?	A. Highly likely benign B. Highly likely malignant C. More likely benign D. More likely malignant E. Not mentioned/No mass
13.	What is the Most Likely Nature of the Renal Mass?	A. Malignant Tumor B. Angiomyolipoma (AML) C. Cyst D. Other Benign Lesion E. Not mentioned/No mass
14.	Invasion of Renal Pelvis/Calyces/Renal Sinus/Peripelvic Fat?	A. Yes B. No C. Not mentioned/No mass

Supplementary Data Table 35: LLM prompt for renal mass feature extraction.

```
# Context
You are a radiologist assisting in extracting information from imaging reports. Please carefully
read the following imaging report and provide appropriate answers to the questions.

# Task
Imaging Report: {}

# Question
Note: If the answer to any question cannot be obtained from the imaging report, please select
DK (Don't Know).

0. Is a renal mass mentioned in the report (including cysts, benign lesions, or malignant lesions)?
If so, is it located in the left kidney, right kidney, or bilateral?
A. Left kidney B. Right kidney C. Bilateral kidneys D. Not mentioned

Then, for each identified renal mass, please answer the following questions (full details and
options for each question are provided in Supplementary Data Table 33 and Supplementary
Data Table 34):

1. Overall Nature and Number
2. Location within Kidney
3. Size
4. Exophytic Type?
5. Morphology
6. Cystic or Solid Nature
7. Density/Signal Intensity
8. Evidence of Necrosis?
9. Enhancement Pattern (Overall)
10. Enhancement (Arterial Phase)
11. Margins Clarity
12. Likely Benign or Malignant?
13. Most Likely Nature?
14. Invasion of Renal Pelvis/Sinus/Peripelvic Fat?

Prefix the question number with L (e.g., L1) for answers pertaining to the left kidney mass.
Prefix the question number with R (e.g., R1) for answers pertaining to the right kidney mass.

# Format
Please provide your answer in JSON format, structured as follows:
{
  0: "...",
  L1: "...",
  ...,
  L14: "...",
  R1: "...",
  ...,
  R14: "..."
}
Only provide the letter corresponding to the answer choice; do not include the question descrip-
tion or answer options.

# Result
```

Supplementary Data Table 36: Hyperparameters for image backbone pre-training. Training was conducted on a single 80GB NVIDIA A100 GPU for up to 200 epochs. The best-performing model checkpoint was selected based on the highest macro-averaged AUC on the pre-training dataset’s validation set, reflecting its performance across multiple classification tasks.

Hyperparameter	Value
Batchsize	300
Learning rate	5e-4
Weight Decay	5e-3
AdamW β	(0.9,0.999)
Learning rate schedule	Cosine
Warmup ratio	10%
Epochs	200

Supplementary Data Table 37: Hyperparameters for text encoder pre-training in the MLM phase. This phase was conducted on a single 80GB NVIDIA A100 GPU for up to 1,000 iterations.

Hyperparameter	Value
Layers	32
Heads	32
Embedding dimension	4,096
Hidden dimension	14,336
Position embedding	RoPE
Vocabulary size	128,256
Batchsize	32
Learning rate	5e-5
MLM probability	0.2
LoRA alpha	16
LoRA scale	32
LoRA dropout	0.05
Weight Decay	0
AdamW β	(0.9,0.999)
Learning rate schedule	Linear
Automatic mixed precision	bf16
Gradient checkpointing	✓
Iterations	1,000

Supplementary Data Table 38: Hyperparameters for text encoder pre-training in the SimCSE phase. This phase was conducted on a single 80GB NVIDIA A-100 GPU for up to 1,000 iterations.

Hyperparameter	Value
Layers	32
Heads	32
Embedding dimension	4,096
Hidden dimension	14,336
Position embedding	RoPE
Vocabulary size	128,256
Batchsize	128
Learning rate	3e-5
SimCSE dropout	0.2
LoRA alpha	16
LoRA scale	32
LoRA dropout	0.05
Weight Decay	0
AdamW β	(0.9,0.999)
Learning rate schedule	Linear
Automatic mixed precision	bf16
Gradient checkpointing	✓
Iterations	1,000

Supplementary Data Table 39: Training hyperparameters for cross-modal pre-training. Experiments were conducted on four NVIDIA A100 80GB GPUs, utilizing a local batch size of 1,024 per GPU with mixed-precision training for enhanced efficiency. Training proceeded for up to 100 epochs, with the best-performing model checkpoint selected based on the highest cross-modal retrieval recall observed on the pre-training dataset’s validation set.

Hyperparameter	Value
Batch size per GPU	1,024
Image backbone learning rate	1e-5
Projection head learning rate	5e-4
Weight Decay	1e-2
AdamW β	(0.9,0.98)
Learning rate schedule	Cosine
Warmup ratio	10%
Epochs	100
Automatic mixed precision	bf16
Temperature	Learnable
Gradient clipping max norm	0.2

Supplementary Data Table 40: Data augmentation techniques for 3D CT volumes.

Augmentation	Description	Probability	Parameters/Range
Random Crop	Randomly crop a sub-volume from the input.	1.0	From (140, 140, 32) to (128, 128, 32)
Translation	Randomly shift the 3D data along the X and Y axes.	1.0	$[-10, 10]$ pixels
Rotation	Randomly rotate the 3D data around the X, Y, and Z axes.	1.0	$[-\frac{\pi}{10}, \frac{\pi}{10}]$ radians
Scaling	Randomly scale the 3D data along the X and Y axes.	1.0	$[0.9, 1.1]$
Horizontal Flip	Flip the 3D data along the X-axis. ^a	0.5	-
Intensity Scaling	Randomly scale image intensity.	1.0	$[0.9, 1.1]$
Intensity Shift	Randomly shift image intensity by adding an offset.	1.0	$[-0.1, 0.1]$
Contrast Adjustment	Randomly change image intensity using gamma transformation.	0.5	$(0.5, 2.0)$

^aTo maintain semantic consistency in image-text pairs (e.g., preserving left/right anatomical distinctions), horizontal flipping was applied only during fine-tuning for specific downstream tasks and excluded from the pre-training phase.

Supplementary Data Table 41: Training hyperparameters for radiology report generation (Step 1). For the initial training step, which focused solely on optimizing the multi-modal projector while the image encoder and LLM remained frozen, a single 80GB NVIDIA A100 GPU was utilized. Training proceeded for up to 20 epochs, with the best-performing model checkpoint selected based on the lowest validation loss observed on the pre-training dataset’s validation set.

Hyperparameter	Value
Batchsize	30
Learning rate	1e-3
Weight Decay	5e-2
AdamW β	(0.9,0.999)
Learning rate schedule	Cosine
Warmup ratio	10%
Epochs	20

Supplementary Data Table 42: Training hyperparameters for radiology report generation (Step 2). This fine-tuning step built upon the initial pre-training setup, focusing on optimizing the multi-modal projector and fine-tuning the LLM (BioMistral-7B) using LoRA. Training was conducted on a single 80GB NVIDIA A100 GPU. The maximum sequence length for captions was set to 256, a length chosen as the majority of reports in the dataset were shorter than this.

Hyperparameter	Value
Layers	32
Heads	32
Embedding dimension	4,096
Hidden dimension	14,336
Position embedding	RoPE
Vocabulary size	32,000
Max sequence length	256
Batchsize	30
Projector learning rate	5e-4
LoRA weights learning rate	2e-6
LoRA alpha	4
LoRA scale	4
LoRA dropout	0.2
Weight Decay	5e-2
AdamW β	(0.9,0.999)
Learning rate schedule	Cosine
Warmup ratio	10%
Epochs	2